J. Fluid Mech. (1994), *vol.* 271, *pp.* 351–378

Streaming flows due to g-jitter-induced natural convection

By A. FAROOQ[1] AND G. M. HOMSY[2]

[1] Department of Mechanical Engineering, Stanford University, Stanford, CA 94305, USA

[2] Department of Chemical Engineering, Stanford University, Stanford, CA 94305, USA

(Received 14 April 1992 and in revised form 5 January 1994)

We investigate streaming in a square cavity where a lateral temperature gradient interacts with a constant gravity field modulated by small harmonic oscillations of order ϵ. The Boussinesq equations are expanded by regular perturbation in powers of ϵ, and the $O(\epsilon^2)$ equations contain Reynolds-stress-type terms that cause streaming. The resulting hierarchy of equations is solved by finite differences to investigate the $O(\epsilon^1)$ and $O(\epsilon^2)$ fields and their parametric dependence on the Rayleigh number Ra, Prandtl number Pr, and forcing frequency ω. It has been found that the streaming flow is quite small at small values of Ra, but becomes appreciable at high Ra and starts to influence such flow properties as the strength of the circulation and the overall heat transfer. Under suitable parametric conditions of finite frequency and moderate Pr the periodic forcing motion interacts with the instabilities associated with the $O(\epsilon^0)$ base flow leading to resonances that become stronger as Ra increases. It is argued that these resonances will have their greatest effect on streaming for $Pr \approx 1$. At low frequencies the streaming flow shows marked structural changes as Ra is increased leading to an interesting change in the sign of the $O(\epsilon^2)$ contribution to the Nusselt number. Also, as the frequency is changed the $O(\epsilon^2)$ Nusselt number again changes sign at approximately the resonant frequency.

1. Introduction

A well-understood problem in buoyancy-driven convection is the flow induced in a Boussinesq fluid by a lateral temperature gradient in the presence of a constant downward gravitational field. This problem has been the subject of several numerical, analytic and experimental treatments and a good introduction can be found in Gebhart *et al.* (1988). In the present work we wish to introduce a more general gravitational forcing which may have arbitrary spatial and temporal dependence, i.e. if $\boldsymbol{g}$ denotes this generalized gravity, we have $\boldsymbol{g} = \boldsymbol{g}(\boldsymbol{x}, t)$. For small cavities it is reasonable to assume that $\boldsymbol{g}$ has a spatially uniform time-averaged component, permitting us to write it as

$$\boldsymbol{g} = g_0(\boldsymbol{k} + \epsilon \boldsymbol{f}(\boldsymbol{x}, t)), \tag{1}$$

where g_0 is the time-averaged value of $\boldsymbol{g}$ acting along the direction of the unit vector $\boldsymbol{k}$ and $\boldsymbol{f}(\boldsymbol{x}, t)$ is any arbitrary vector; ϵ is a scaling parameter which gives the magnitude of the forcing vector $\boldsymbol{f}(\boldsymbol{x}, t)$ relative to the magnitude of the mean gravity g_0. If $\epsilon \ll 1$ then the forcing may be seen as a perturbation of the mean gravity. Since the governing equations are nonlinear this kind of forcing leads to the phenomenon of streaming, where a time-periodic forcing with zero mean produces a periodic response consisting of a steady solution with a non-zero mean and time-dependent fluctuations involving

higher harmonics. This streaming field is significant because it can contribute to various transport phenomena such as heat transfer or the distribution of chemical species in a time-averaged sense.

The first theoretical analysis of the phenomenon of streaming was done by Lord Rayleigh (1945), in connection with sound waves. Later Schlichting (1979) solved for the streaming flow field produced by radial oscillations of a cylinder in an infinite fluid. Lighthill (1978) has clarified the mechanisms responsible for streaming by focusing on the production of Reynolds-stress-type terms that contribute to the mean transport. More recently, there is renewed interest in the subject due to g-jitter-induced streaming produced in microgravity environments. Alexander (1990) has discussed the significance of g-jitter in understanding space experiments where buoyancy forces play a role. Biringen & Peltier (1990) have investigated g-jitter effects on three-dimensional Rayleigh–Bénard convection by considering the full nonlinear time-dependent problem. Their results agree with the earlier linearized treatment of Gresho & Sani (1970) who reduced the Rayleigh–Bénard system to a problem governed by Mathieu's equation. Thus, depending on the frequency of the forcing, the system exhibits a synchronous or subharmonic response. Biringen & Danabasoglu (1990) have solved the full nonlinear, time-dependent Boussinesq equations for g-jitter in rectangular cavities. The part of their results relevant here is that obtained for non-zero terrestrial gravity and modulation that is perpendicular to the applied temperature gradient. Although in their work the modulation is much larger than the time-averaged gravity ($\epsilon = 19.6$, ϵ defined previously) their result shows the response to consist of a harmonic time-dependent component superposed over steady streaming. Our results are complementary to these, since by a weak nonlinear calculation, we are able to explore parametric dependencies that explain physical mechanisms and scalings. Amin (1988) has investigated the heat transfer from a sphere immersed in an infinite fluid medium in a zero-gravity environment under the influence of g-jitter. Her conclusion is that heat transfer is negligible for high-frequency g-jitter but under special circumstances, when the Prandtl number is high enough, low-frequency g-jitter may play an important role. Alexander *et al.* (1991) have carried out a numerical investigation of the effect of g-jitter on dopant concentration in a modelled crystal growth reactor. They conclude that low-frequency g-jitter can have a significant effect on dopant concentration.

The focus of this study is to examine the response of a nonlinear system, such as one consisting of an enclosed Boussinesq fluid with an imposed temperature gradient, to a time-periodic perturbation of the gravitational field, $\boldsymbol{g}$ as given by (1). By considering a small perturbation of the gravitational field, the equations can be expanded in powers of ϵ, leading to results of great simplicity that can be interpreted to understand the mechanisms of streaming. Since the problem is governed by no fewer than four parameters, and there are a number of physical mechanisms operative in various regimes of this parameter space, we feel that the semi-analytic approach adopted here, while limited to small ϵ, yields insight and understanding that would be difficult to obtain otherwise. Our initial interest is in streaming flows caused by forcings that are periodic and aligned with the steady gravitational field and a temperature gradient that is normal to the direction of the gravitational field. In this work, §2 describes the problem geometry and the small-ϵ expansions of the Boussinesq equations. Section 3 considers the techniques employed to solve the equations and also a discussion of numerical accuracy. In §4 we present the results in the special limit of very low-forcing frequency – the quasi-static approximation – and in §5 we consider the case of finite forcing frequencies. In the course of finite-frequency studies, it is useful to recall the extensive literature on instability modes of the unforced system. We review that

literature in the appropriate sections. Section 6 contains suggestions for extensions to the present work.

2. Problem definition

Figure 1 shows the geometry considered, i.e. a square two-dimensional cell of side L. The cell contains a Boussinesq fluid and the temperature of the two lateral walls is assumed to be T_1 and T_0, where $T_1 > T_0$, the other two walls being thermally insulated. No-slip boundary conditions and impermeability of all walls has also been assumed. A time-dependent body force in accord with (1) acts on the fluid and, as a result of volume expansion, fluid circulation will exist. In order to scale the equations we choose thermal-diffusive time and velocity scalings:

$$\theta = \frac{T-T_0}{\delta T}, \quad \boldsymbol{U} = \frac{\boldsymbol{V}}{\kappa/L}, \quad \tau = \frac{t}{L^2/\kappa}, \quad \omega = \frac{wL^2}{\kappa},$$

where $\delta T = T_1 - T_0$, κ is the thermal diffusivity and w is the frequency of any of the Fourier modes into which (1) may be decomposed. In this initial study we confine ourselves to the case where the gravitational perturbation is aligned with the steady gravitational field acting downward. Hence if unit vector $\boldsymbol{k}$ is chosen to be along the positive y-axis, (1) can be rewritten as

$$\boldsymbol{g} = -g_0[1 + \epsilon f(\tau)]\boldsymbol{k}, \tag{2}$$

where f is assumed to be a function of time only. For now we consider the case of a harmonic forcing where f is given by $f(\tau) = \cos(\omega\tau)$ and ω is the (single) dimensionless forcing frequency. Later, in §6 we consider the case of a general $f(\tau)$. The full time-dependent Boussinesq equations thus assume the form

$$\nabla^4\psi - \frac{1}{Pr}[\partial_\tau \nabla^2\psi + J(\psi, \nabla^2\psi)] = Ra\,\partial_x\theta[1 + \epsilon\cos(\omega\tau)], \tag{3}$$

$$\partial_\tau\theta + J(\psi, \theta) = \nabla^2\theta, \tag{4}$$

where $Pr = \nu/\kappa$ is the Prandtl number, and the Rayleigh number Ra is defined as $Ra = \alpha(\delta T)g_0 L^3/(\nu\kappa)$; ν is the kinematic viscosity, α the volume expansion coefficient. $J(u, v)$ is defined as $J(u, v) = u_y v_x - u_x v_y$. The following boundary conditions are applied: the streamfunction is zero at all boundaries as is its normal derivative. The temperature boundary conditions are $\theta(0, y) = 1$, $\theta(1, y) = 0$ and $\theta_y(x, 0) = \theta_y(x, 1) = 0$.

For reasons noted above, it is compelling to consider the $\epsilon \ll 1$ limit wherein the Boussinesq equations can be expanded in powers of ϵ. We therefore have

$$\psi = \psi_0 + \epsilon\psi_1 + \epsilon^2\psi_2 + \ldots,$$
$$\theta = \theta_0 + \epsilon\theta_1 + \epsilon^2\theta_2 + \ldots.$$

When these expansions are substituted into (3) and (4), they generate a hierarchy of equations to be solved at each order of ϵ. At $O(\epsilon^0)$ we recover the steady Boussinesq equations for a stationary gravitational field with ψ replaced by ψ_0 and θ replaced by θ_0. The boundary conditions are the same as before. We thus have

$$\nabla^4\psi_0 - \frac{1}{Pr}J(\psi_0, \nabla^2\psi_0) = Ra\,\partial_x\theta_0, \tag{5}$$

$$\nabla^2\theta_0 = J(\psi_0, \theta_0). \tag{6}$$

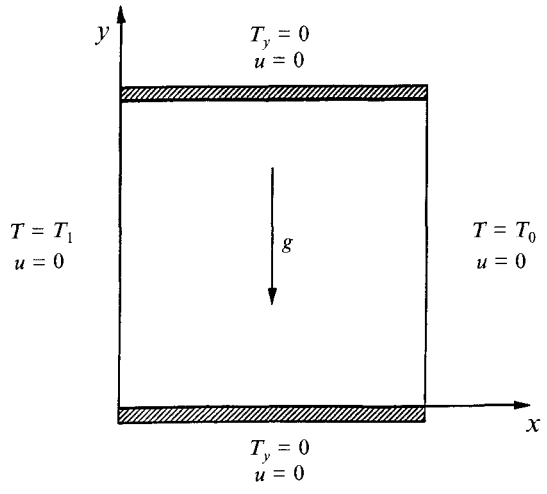

FIGURE 1. Geometry of the flow showing boundary conditions.

Thus the $O(\epsilon^0)$ problem with associated non-homogeneous boundary conditions is the well-studied problem of thermal convection in a horizontally heated cavity, which we refer to as the base state. Higher-order terms, which are time dependent, are perturbations of this stationary base-state solution. We have at each $O(\epsilon^n)$, where $n = 1, 2, \ldots$, linear systems of equations for streamfunction and temperature with boundary conditions that are homogeneous. These equations can be written very compactly in terms of the operators $\mathscr{L}_\psi$ and $\mathscr{L}_\theta$:

$$\mathscr{L}_\psi(\psi_i, \theta_i) = \nabla^4\psi_i - \frac{1}{Pr}(J(\psi_0, \nabla^2\psi_i) + J(\psi_i, \nabla^2\psi_0)) - Ra\,\partial_x\theta_i, \tag{7}$$

$$\mathscr{L}_\theta(\psi_i, \theta_i) = \nabla^2\theta_i - J(\psi_0, \theta_i) - J(\psi_i, \theta_0), \tag{8}$$

where $i = 1, 2$ and ψ_i stands for the streamfunction at ith order of ϵ. Hence it is possible to view these as linear systems of the type

$$\partial_\tau \mathscr{A}(\psi_n, \theta_n) + \mathscr{L}(\psi_n, \theta_n) = \boldsymbol{h}_n(\boldsymbol{x}, \tau)$$

for $n = 1, 2$ where $\mathscr{L}, \mathscr{A}$ are linear operators given by

$$\mathscr{L}(\psi_n, \theta_n) = \begin{pmatrix} \mathscr{L}_\psi(\psi_n, \theta_n) \\ \mathscr{L}_\theta(\psi_n, \theta_n) \end{pmatrix}, \quad \mathscr{A}(\psi_n, \theta_n) = \begin{pmatrix} -(1/Pr)\nabla^2\psi_n \\ -\theta_n \end{pmatrix},$$

and $\boldsymbol{h}_n$ represents the forcing on the right-hand side. At first order in ϵ the forcing, $\boldsymbol{h}_1$, can be written as $\boldsymbol{h}_1 = \boldsymbol{h}_1'(\boldsymbol{x})\,e^{i\omega\tau}$; hence we have particular solutions for ψ_1 and θ_1 (at long times) of the form

$$\psi_1 = \mathrm{Re}[\psi_1' e^{i\omega\tau}], \quad \theta_1 = \mathrm{Re}[\theta_1' e^{i\omega\tau}].$$

Substituting $\psi_1 = \psi_1' e^{i\omega\tau}$, etc. into the $O(\epsilon^1)$ terms, simplifying and dropping the primes for notational brevity gives the following equations for the $O(\epsilon^1)$ fields:

$$-\frac{i\omega}{Pr}\nabla^2\psi_1 + \mathscr{L}_\psi(\psi_1, \theta_1) = Ra\,\partial_x\theta_0, \tag{9}$$

$$-i\omega\theta_1 + \mathscr{L}_\theta(\psi_1, \theta_1) = 0. \tag{10}$$

ψ_1 and its normal derivatives are zero on the boundaries. θ_1 is zero on the lateral walls and its normal derivatives are zero on the upper and lower walls. At $O(\epsilon^2)$, the forcing

terms consist of a steady-streaming component and a time-dependent higher harmonic due to generalized Reynolds-stress terms. As before we can express particular solutions to the linear system as

$$\psi_2 = \psi_2' + \psi_2^* \, e^{2i\omega\tau}, \quad \theta_2 = \theta_2' + \theta_2^* \, e^{2i\omega\tau}.$$

Substituting these into the $O(\epsilon^2)$ terms and simplifying, it is possible to extract two sets of equations: one for the time-dependent higher harmonic, which is not of interest here, and another system for the steady streaming component:

$$\mathscr{L}_\psi(\psi_2, \theta_2) = \frac{1}{2}\left[Ra\, \partial_x \theta_1 + \frac{1}{Pr}(J(\psi_1^R, \nabla^2\psi_1^R) + J(\psi_1^I, \nabla^2\psi_1^I)\right], \tag{11}$$

$$\mathscr{L}_\theta(\psi_2, \theta_2) = \tfrac{1}{2}[J(\psi_1^R, \theta_1^R) + J(\psi_1^I, \theta_1^I)], \tag{12}$$

where the superscripts R, I denote the real and imaginary parts respectively. Again, we have dropped the primes for notational convenience. The homogeneous boundary conditions for ψ_2 and θ_2 are identical to those at $O(\epsilon)$. These coupled sets of equations, (5), (6) and (9)–(12), with appropriate boundary conditions can be solved sequentially to obtain the base state and its higher-order corrections. It is seen that the solution depends upon three parameters: Ra, Pr and the dimensionless forcing frequency, ω. While carrying out the ϵ-expansions it is seen that the perturbation to gravity is multiplied by Ra making it a term of scale $\epsilon\, Ra$. Hence caution is needed when taking the limit $Ra \to \infty$ which is often of interest, because in order to ensure the validity of the expansion, $\epsilon\, Ra \ll 1$ should be enforced even as $Ra \to \infty$.

As mentioned earlier, the $O(\epsilon^0)$ problem is well studied and has been described in analytic studies such as Batchelor (1954) where the conduction regime at low Ra is considered and Gill (1966) where boundary-layer behaviour is considered at high Ra. There are numerical studies such as Vahl Davis (1968) and the more recent work of Chenoweth & Paolucci (1986). There are a number of experimental studies as well, for example by Elder (1965). These studies establish that at low Ra the flow is weak and the heat transfer is dominated by conduction. At high Ra the flow becomes stronger, resulting in buoyancy boundary layers on the sidewalls and a vertically stratified inner core.

Equations (9) and (10) represent forced linear systems. If we consider the corresponding homogeneous equations along with homogeneous boundary conditions, they constitute an eigenvalue problem which would give a set of eigenvalues and eigenvectors that would correspond to modes of instability of the base-state flow. In particular (9) and (10) for natural modes become

$$\mathscr{L}_\psi(\psi_1, \theta_1) = \frac{i\lambda}{Pr}\nabla^2\psi_1, \tag{13}$$

$$\mathscr{L}_\theta(\psi_1, \theta_1) = i\lambda\theta_1, \tag{14}$$

where λ is the complex eigenvalue for normal modes proportional to $e^{i\lambda\tau}$. This is an interesting problem, which because of the complexity of the variable coefficients has not been completely dealt with in the literature. However, a fairly complete analysis of model problems together with direct numerical simulations allow us to understand the basic instability mechanisms that are associated with the eigenvalue problem, (13) and (14). Gill & Davey (1969) and Bergholz (1978) have studied a model problem in which the walls of a channel of width L but infinite vertical dimension are held at temperatures $T = \Delta T + Gy$ and Gy respectively. These boundary conditions admit an exact parallel-flow solution of the Boussinesq equations whose stability depends upon

the Rayleigh and Prandtl numbers and upon the dimensionless stratification parameter, $\gamma_B = (\frac{1}{4}\tau_B Ra)^{1/4}$, where $\tau_B = (GL/\Delta T)$ (the subscript B denotes variables in Bergholz's 1978 scaling). The results are complicated in detail but the following general picture applies: for small Pr there exists a stationary mode that is driven by buoyancy. As γ_B increases, the base-state profiles tend towards boundary-layer limits, and the stationary mode is replaced by travelling modes. Competition between these modes exists for $0 < Pr < 12.7$. In the range $12.7 < Pr < 50$, only travelling modes occur, but for $Pr > 50$ there is again competition between modes with large γ_B again favouring the travelling waves. The travelling wave is the only mode to survive in the boundary-layer limit $\gamma_B \to \infty$. Numerical results are available over the entire range of parameters (Bergholz 1978) and rescaled results and asymptotic formulae are available in the single buoyancy-layer limit, $\gamma_B \to \infty$, in Gill & Davey (1969).

Attempts to relate these instabilities observed in experiments in closed cavities of finite aspect ratio require an estimate of the stratification parameter G as a function of Ra, Pr and aspect ratio A, and the assumption that the stability problem is adequately treated by a local parallel-flow approximation. When G is estimated for large Ra from the boundary-layer theory of Gill (1966), reasonably good agreement is found over a range of Pr for tall cavities, see e.g. Bergholz (1978, table 4).

The results of relevance here are for the travelling wave modes at high Ra, these being associated with both shear and buoyancy modes within the boundary layer. In the present scalings, these layers are expected to become unstable at Rayleigh numbers, Ra_{BL},

$$Ra_{BL} = (\hat{R}Pr)^4/2A^3, \tag{15}$$

where $\hat{R}$ is a Reynolds-number based on the velocity in the buoyancy layer and A is the aspect ratio of the cavity, which in our case is 1. Gill & Davey (1969) tabulate the critical value of $\hat{R}$ as a function of Pr for boundary-layer instability. In the limit $Pr \to \infty$, this becomes (using values from Gill & Davey 1969) $Ra_{BL} = 25312.5Pr^2/A^3$. The frequency of the neutral travelling modes is given by

$$\omega_{BL} = \hat{\alpha}\hat{c}Ra^{3/4}(8A)^{1/4}. \tag{16}$$

Again the $\hat{\alpha}, \hat{c}$ are the wavenumber and phase velocity of the critical mode which are tabulated in Gill & Davey (1969). There are other modes associated with internal waves in the stably stratified core. A number of workers have studied the problem of transient flow in a heated cavity in what has also been called the 'oscillatory approach to steady state'. Here a sudden large temperature gradient is applied to the cavity at some initial time and the velocity and temperature fields in the cavity are treated as an initial-value problem. The initial perturbation excites transient modes which are damped out as the flow approaches steady state, suggesting an oscillatory relaxation process. Patterson & Imberger (1980) consider this to be a result of the rapid turning of a hot (cold) packet of fluid as it reaches the top (bottom) wall of the cavity. This is thought to cause a tilting of isotherms, exciting gravity waves which oscillate at the Brunt–Väisälä frequency. Using scale analysis Patterson & Imberger (1980) have predicted that the time required for transients to die out scales as $Ra^{-1/4}$. This is interesting because it provides an estimate of the time when the solution of (9) and (10) would become purely harmonic.

Ivey (1984) has conducted experiments on impulsively heated (cooled) cavities and observed such wave motion. He suggests that such motion is excited by an unstable hydraulic jump which forms if the Froude number of the flow after turning the corner is supercritical. The condition for the formation of such unstable jumps may be established by a combination of scaling analysis and adoption of a criterion for

instability of the jump. In the present scalings, the instability of the internal wave occurs when

$$Ra_{GW} > 1.3 \times 10^8 Pr^4/A^3 \tag{17}$$

and with a characteristic Brunt–Väisälä frequency

$$\omega_{GW} = \left(\frac{1}{2A} Ra\, Pr\right)^{1/2}. \tag{18}$$

It should be emphasized that (15)–(18) imply a specific choice of stratification at high Ra, i.e. $\tau_B = \frac{1}{2}A^{-1}$.

These concepts have been fully validated through extensive direct numerical simulations of Paolucci & Chenoweth, who studied time-dependent two-dimensional thermal convection for a specific Prandtl number ($Pr = 0.71$) over a range of aspect ratios and Rayleigh numbers. They find two distinct stability modes whose transitional Rayleigh numbers and frequencies are well predicted by (15)–(18): for Rayleigh numbers below that given by (15) and (17) they find damped modes with frequencies corresponding to (16) and (18). They also present a number of time sequences showing how the hydraulic jumps at the top (hot) and lower (cold) corners become oscillatory and excite internal waves in the stratified core. We note that the local scale analysis of Patterson & Imberger (1980) is incapable of showing sustained oscillations, as it neglects coupling between the local excitation in the corners and the overall fluid circulations. Paolucci & Chenoweth (1989) make this connection through numerical simulations and an appeal to the forced mixing experiments of Thorpe (1968).

These oscillatory modes associated with boundary-layer travelling-wave instabilities and excited internal waves will become relevant to our studies in §5 which involve forcing at finite frequency.

Now we may ask what the forced problem, given by (9) and (10) represents and what kind of solutions can we expect for it. It is clear that if the forcing term on the right-hand side corresponds exactly to the eigenvector at the corresponding frequency, this would result in a resonance which would make (9) and (10) singular. However, it is highly unlikely that the forcing would be exactly the same as the eigenvector. More generally we would expect to have for a given choice of (Ra, Pr, ω) a non-zero projection along the eigenvector that is 'nearest' the given forcing. This eigenmode would become excited leading to a response that would depend on the eigenvalues of (13) and (14). Suppose we are in a parametric regime (Ra, Pr) where all the eigenvalues of the homogeneous problem have negative real parts and thus represent damped modes: in other words the unforced problem is linearly stable. Then we can expect interactions with the forcing which might lead to enhanced circulation/heat transfer. As the eigenvalues become positive (to be expected at very high Ra) we expect large resonances but the solution is suspect since the assumed (steady) flow is itself unstable.

3. Numerical method

We give here a brief discussion of our numerical method and its accuracy. We have three coupled systems of elliptic partial differential equations, (5) and (6), (9) and (10), and (11) and (12), which we solved successively at each order in ϵ using finite differences. The $O(\epsilon^0)$ equations are nonlinear and must be solved iteratively. Because of the variable coefficients and forcing, the $O(\epsilon^1)$ and $O(\epsilon^2)$ equations also have to be treated numerically, but being linear systems they can be solved either iteratively or by direct inversion of the matrix resulting from finite differencing. We used standard

Grid size	Nu_0	Nu_2	$\lvert\psi_0\rvert_{max}$	$\lvert\psi_1\rvert_{max}$	$\lvert\psi_2\rvert_{max}$
16×16	1.083	1.587×10^{-2}	1.055	9.072×10^{-1}	7.010×10^{-2}
31×31	1.112	1.660×10^{-2}	1.146	9.897×10^{-1}	7.984×10^{-2}
61×61	1.116	1.654×10^{-2}	1.167	1.006×10^{-0}	8.084×10^{-2}

TABLE 1. Effect of grid size on Nusselt number and maximum field properties at $Ra = 10^3$; $Pr\to\infty$; $\omega = 0$

Grid	$\lvert\psi_0\rvert_{max}$	$\lvert\psi_1\rvert_{max}$	$\lvert\theta_1\rvert_{max}$
31×31	17.12%	30.47%	30.48%
41×41	10.29%	12.45%	11.01%
61×61	3.14%	6.47%	1.89%

TABLE 2. Percent error in $\lvert\psi_0\rvert_{max}$, $\lvert\psi_1\rvert_{max}$ and $\lvert\theta_1\rvert_{max}$ for $Ra = 10^6$; $Pr\to\infty$; $\omega = 0$ with mesh refinement. The error has been calculated using 81×81 solutions as base values. The maximum field values at 81×81 mesh are: $\lvert\psi_0\rvert_{max} = 18.74$; $\lvert\psi_1\rvert_{max} = 6.18$; $\lvert\theta_1\rvert_{max} = 0.1371$

Ra	$\lvert\psi_0\rvert_{max}$ (DVD)	$\lvert\psi_0\rvert_{max}$ (P)	Nu_0 (DVD)	Nu_0 (P)
10^3	—	1.1670 (61×61)	1.118	1.112
10^4	—	5.0280 (31×31)	2.243	2.262
10^5	9.612	10.312 (41×41)	4.519	4.597
10^6	16.32	16.815 (41×41)	8.800	8.694

TABLE 3. Comparison of present (P) results with de Vahl Davis (1982) (DVD) at finite Prandtl number, $Pr = 0.71$

second-order centred differences and enforced the Neumann boundary conditions with one-sided second-order formulae at the boundaries. The calculations for low forcing frequencies were performed using SOR. At large frequencies, the matrix becomes highly unsymmetric and SOR performs poorly. Hence we used a direct sparse solver, see Zlatev, Wasniewski & Schaumburg (1981) which performs full Gaussian elimination making full use of the sparsity of the matrix.

We first consider the accuracy of the solutions for the quasi-static case obtained in the limit $Pr\to\infty$ and $\omega\to0$. We solved the quasi-static equations using point SOR and the convergence criterion used was to reduce the error by a factor of 10^5–10^8 depending upon the parameters. The governing equations at each order of ϵ are invariant with respect to the following transformation: $x^* = -x$; $y^* = -y$; $\psi_i^* = \psi_i$; $\theta_i^* = -\theta$, where $i = 0, 1, 2$. We verified that the numerical solution also showed these symmetries. Table 1 shows the 16×16, 31×31 and 61×61 results for the Nusselt numbers Nu_0 and Nu_2 (Nu_2 to be defined below) and the maximum values of the streamfunctions, $\lvert\psi_0\rvert_{max}$, $\lvert\psi_1\rvert_{max}$ and $\lvert\psi_2\rvert_{max}$ at $Ra = 10^3$, $Pr\to\infty$ and $\omega = 0$.

In table 2 we show further mesh refinement results for $Ra = 10^6$ for meshes of 31×31, 41×41, 61×61 and 81×81. The error was calculated using the 81×81 solution as base. For meshes of 41×41 and higher the error is about 10%.

Next we consider the results for finite Prandtl number and finite frequency. Vahl Davis & Jones (1982) have done bench-mark calculations for the $O(\epsilon^0)$ problem for $Pr = 0.71$. These are presented along with the present results for $Ra = 10^5$ and 10^6 in table 3 which tabulates the maximum value of the streamfunction, $\lvert\psi_0\rvert_{max}$, Nusselt number and the mesh that was used to generate the results. As can be seen, the results agree to within 5–6%.

ω	21×21	31×31	Error %
10^0	2.1296	2.2625	5.87
10^1	2.1346	2.2355	4.53
10^2	3.6640	3.7561	2.42
10^3	4.8245	4.9440	2.41
10^4	2.1866	2.2733	3.81
10^5	0.3034	0.3252	6.70

TABLE 4. Maximum values of ψ_1 for $Ra = 10^4$; $Pr = 100$ for meshes of 21×21 and 31×31

Grid	$\omega = 1$	$\omega = 20000$
41×41	6.8717	33.62
51×51	7.2993	35.83
61×61	8.1724	39.70

TABLE 5. Effect of mesh refinement on $|\psi_1|_{max}$ at $Ra = 10^7$

The accuracy for finite ω was also studied by mesh refinement. For example, table 4 compares the maximum value of the streamfunction ψ_1 calculated on a mesh of 21×21 and 31×31 for $Ra = 10^4$, $Pr = 100$ at selected values of ω. The table shows a general level of accuracy on the order of 7% or better. In table 5 we show mesh refinement results for $Ra = 10^7$, the highest Ra considered, at meshes of 41×41, 51×51 and 61×61 for $\omega = 1$ and $\omega = 20000$. Although the accuracy degrades at such high Ra, it remains at 15% or better, and the solution shows convergence under mesh refinement. As expected, finer meshes at higher Ra show somewhat slower convergence owing to the well-known stiffness of the governing equations and the onset of boundary-layer behaviour. However, we verified by detailed examination of the full computed fields that even though accuracy was 10–15% all dynamically significant processes were being captured by the numerical resolution employed. To summarize, we utilized grids ranging from 41×41 to 81×81 depending on the parameter values of Ra, ω and Pr with all results accurate to at least 15%, and in most cases better than 5%.

4. The quasi-static approximation

We recall that the response of the system is given by forced linear systems. The forcing, given by the right-hand sides of (9)–(12), has both spatial structure and temporal dependence. In this section we will focus on the effects of the former, i.e. the spatial structure, and consider the limit $\omega \to 0$; in a later section we will examine the more complex case when the system is forced at finite frequencies. In the $\omega \to 0$ limit, the effects associated with temporal rate of change in (9)–(12) are negligible and hence, as we will see, diffusive mechanisms dominate. Furthermore previous studies, e.g. Alexander *et al.* (1991), have suggested that lower frequencies are more significant for enhanced transport due to streaming.

We also invoke the limit $Pr \to \infty$, as this allows us to neglect the nonlinear inertial terms in (11) thus focusing on streaming due to nonlinear convection of energy and correlations of temperature fluctuations with the time-dependent body force. This is a good initial approximation (that will also be relaxed in §5) because numerical computations have shown that the base flow for $Pr \geqslant 1$ is usually quite close to the case of $Pr \to \infty$, see e.g. Vahl Davis (1968). We note that under these limits the perturbation

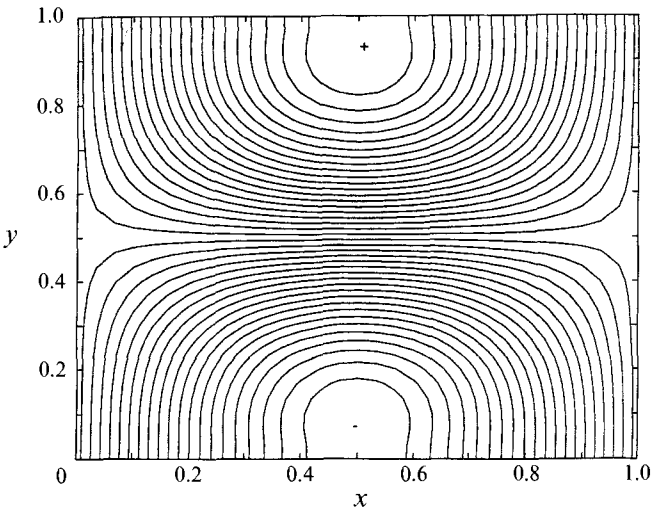

FIGURE 2. Contours of θ_1 at $Ra = 1$ with symmetry about the horizontal midplane. As shown the 'hot' ('cold') contours are at the top (bottom), but this being a sinusoidally oscillating field, the signs are reversed in the latter part of the cycle. The value at the maximum isotherm is 1.544×10^{-3}.

velocity and temperature fields are always in temporal phase with the forcing. We are now left with only one parameter, *Ra*, and can study the dependence on this single parameter in some detail.

4.1. *Numerical results*

In this subsection we examine numerically obtained solutions to (5), (6) and (9)–(12). We find that variations in *Ra*, which is the sole remaining parameter, causes significant structural changes in the response of the system. Further, it is possible to interpret these changes by appealing to the spatial structure of the forcing. This relation is made in subsequent subsections.

Therefore, we begin by considering the behaviour at $Ra = 1$, when the flow is in the conductive regime. It is very well known that the ψ_0 circulation consists of a single cell and the θ_0 isotherms are nearly vertical in this case. The ψ_1 circulation also consists of a single cell and hence is not shown. However, in figure 2 the θ_1 field shows structure, a symmetry about the horizontal midplane, the regions above it being positive and hence hot and the regions below being negative and cold. We recall that the θ_1 field oscillates in time, hence the signs are reversed in the other half of the cycle. Contours of the streaming ψ_2 field shown in figure 3 show a quadrupole structure, diagonally opposite circulations being of the same sign. The lower-left and upper-right cells have a clockwise circulation of the same sense as the ψ_0 field and thus enhance it. The other two cells are of the opposite counterclockwise sense and suppress the ψ_0 circulation. Figure 4 shows the isotherms of the steady θ_2 field which are symmetric about the vertical midplane with the hot (positive) region on the right and the cold (negative) region on the left.

The mean Nusselt number is computed in the usual way by averaging the local flux over the height of the wall for each order of ϵ. Since we are interested in the steady Nusselt number and the θ_1 field does not contribute to the heat transfer in a time-averaged sense, we do not consider it when computing the overall Nusselt number. Hence the Nusselt number is computed as

$$Nu = Nu_0 + \epsilon^2 Nu_2 + O(\epsilon^4), \tag{19}$$

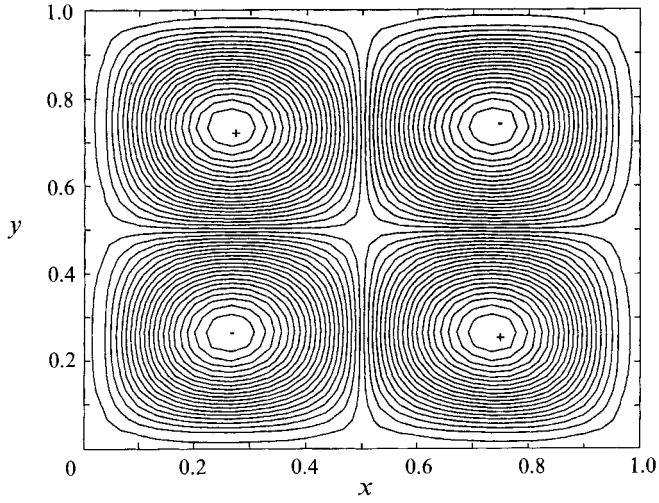

FIGURE 3. Contours of ψ_2 at $Ra = 1$ showing quadrupole streaming. The clockwise (negative) eddies and the counterclockwise (positive) eddies are of approximately the same strength. The maximum value of the streamfunction is 1.4908×10^{-8}.

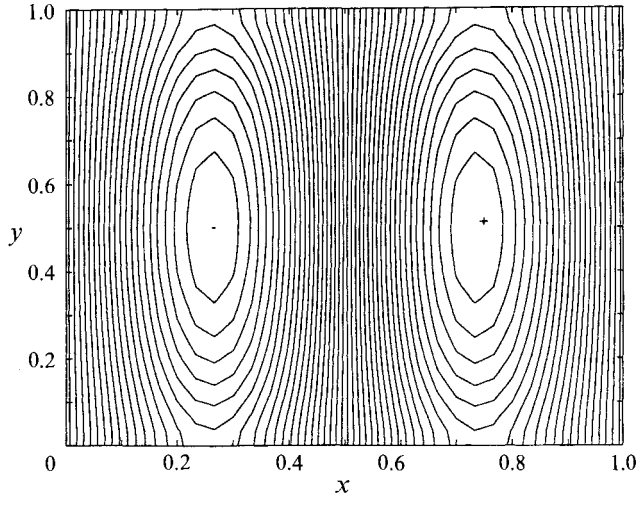

FIGURE 4. Contours of the steady θ_2 field at $Ra = 1$. The hot region is on the right and the cold region is on the left. The value of the maximum isotherm is 1.446×10^{-8}.

Ra	Nu_2	Ra	Nu_2
10^0	6.926×10^{-8}	10^3	1.660×10^{-2}
10^1	6.925×10^{-6}	10^4	-1.357×10^{-1}
10^2	6.822×10^{-4}	10^6	-4.653×10^{-1}

TABLE 6. Variation of Nu_2 with Ra as $\omega \to 0$

where both Nu_0 and Nu_2 are functions of Ra. Table 6 shows numerical values of Nu_2 for a wide range of Ra. As is well known, Nu_0 is near unity at low Ra but increases as Ra is increased. Nu_2 is extremely small at low Ra and increases in magnitude with increase in Ra, but beyond a particular value of Ra, Nu_2 changes sign and continues

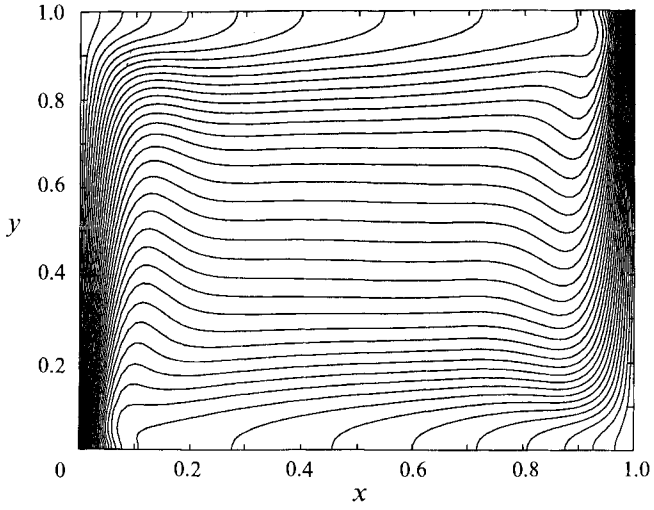

FIGURE 5. Contours of θ_0 at $Ra = 10^6$ showing the thermal boundary layers on the sidewalls and a stably stratified core.

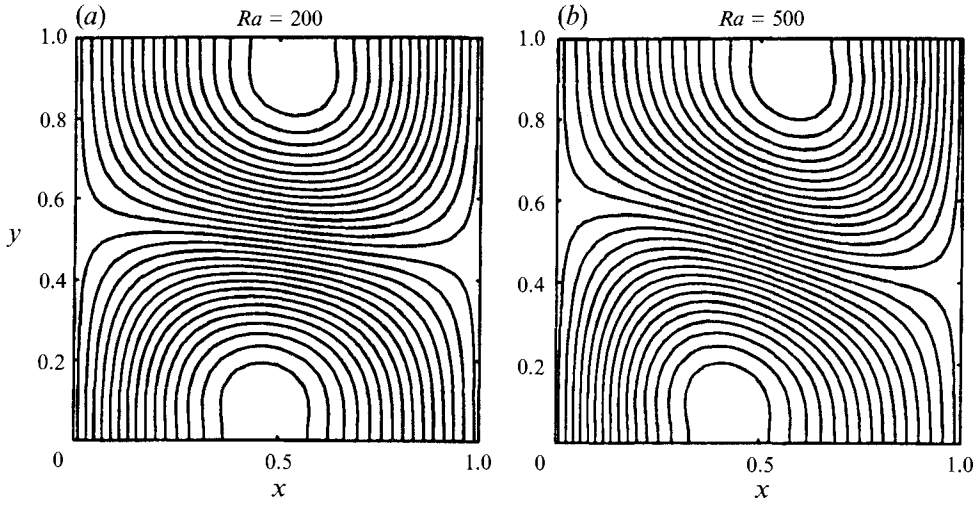

FIGURE 6. Contours of θ_1 at (*a*) $Ra = 200$ and (*b*) 500. It is seen that as Ra is increased the field distorts in a clockwise sense.

to increase in magnitude. Later, we shall see that this is caused by enhanced convection at higher Ra.

Before examining the effect of Rayleigh number on the streaming fields, we briefly consider its effect on the base state and the periodic $O(\epsilon)$ fields. As Ra is increased, the ψ_0 convection cell becomes stronger and at very high Ra, boundary layers form. In the $O(\epsilon^0)$ temperature fields, increase in Ra leads to a distortion of the isotherms due to increase in convective transport of energy and at extremely high Ra leads to thermal boundary-layer behaviour as shown in figure 5 for $Ra = 10^6$. The time-periodic ψ_1 cell, like ψ_0, becomes stronger at higher Ra and forms boundary layers in the limit $Ra \to \infty$. However, the harmonic θ_1 field shows an interesting development, the isotherms begin to distort in a clockwise sense, the extent of the distortion being a function of the

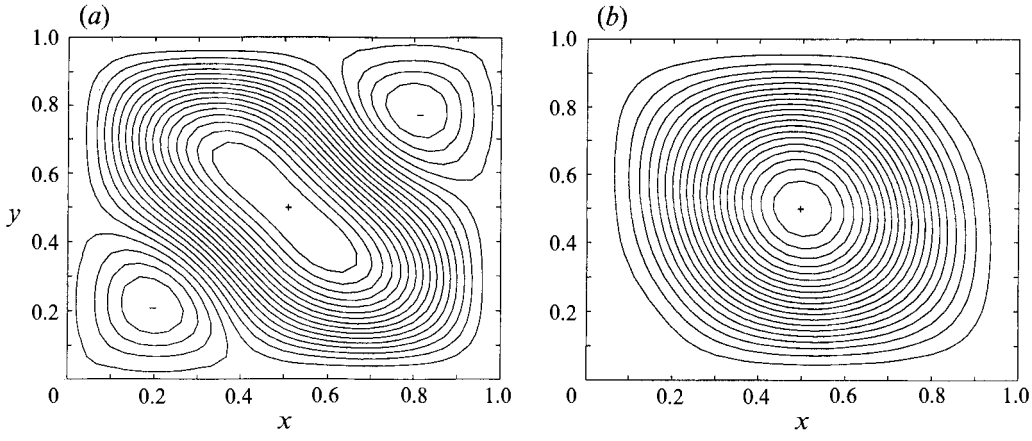

FIGURE 7. (*a*) Contours of ψ_2 at $Ra = 200$ showing suppression of the clockwise rotating eddies. The counterclockwise (positive) eddy is much stronger than at $Ra = 1$, figure 3, the value of the maximum streamfunction being 1.253×10^{-3}. (*b*) Contours of ψ_2 at $Ra = 10^3$ showing a single convection cell which has the opposite sense as the $O(\epsilon^0)$ circulation. The value of the maximum streamfunction is 7.997×10^{-2}.

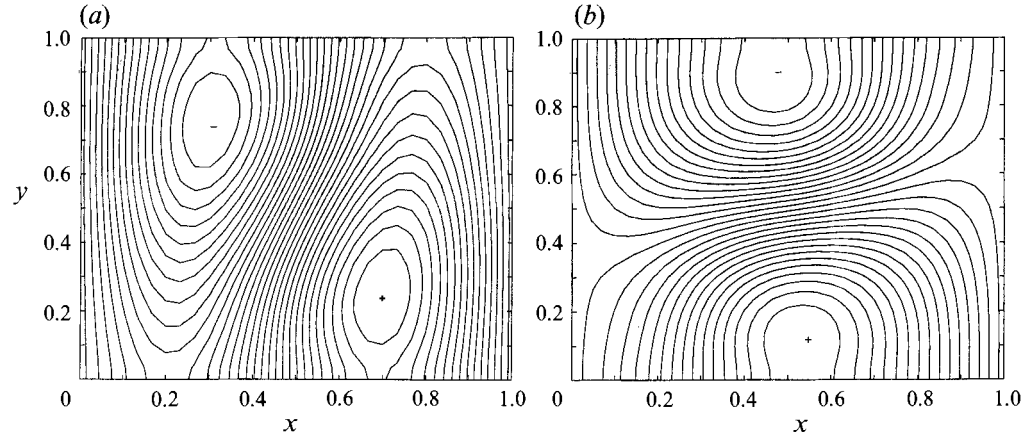

FIGURE 8. (*a*) Contours of θ_2 at $Ra = 200$ showing distortion of isotherms. The value of the maximum isotherm is 6.667×10^{-4}. (*b*) Contours of θ_2 at $Ra = 10^3$ showing progression of distortion with rise in Ra. The value of the maximum isotherm is 1.813×10^{-2}.

Rayleigh number. They are pictured at $Ra = 2 \times 10^2$ and 5×10^2 in figure 6(*a*, *b*) where the distortion can be clearly seen and this progresses as Ra is increased (see also figure 2).

Increasing the Rayleigh number causes a suppression of the two clockwise cells of the quadrupole streaming flow shown in figure 3 whereas the two counterclockwise ones grow in strength and size as shown in figure 7(*a*) for an intermediate Rayleigh number of 200. The two clockwise cells essentially disappear as shown in figure 7(*b*), $Ra = 10^3$, whereas the remaining two coalesce and form a single counterclockwise circulation. This single streaming cell then increases in strength with further increases in Ra. At extremely high Ra, ψ_2 also forms boundary layers.

The θ_2 field which contributes to the average Nusselt number also exhibits very interesting behaviour as shown in figure 8(*a*, *b*). This field begins to distort clockwise with the extent of the distortion being an increasing function of the increase in the Ra:

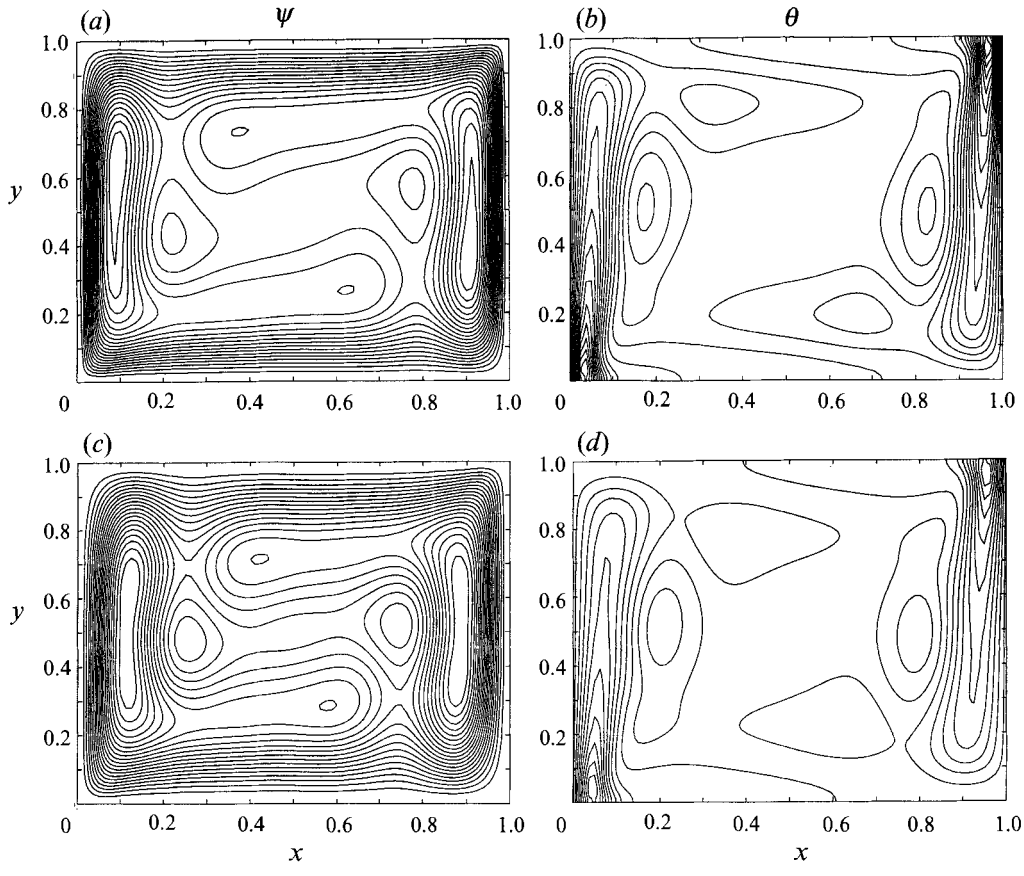

FIGURE 9. Contours of $Ra = 10^6$ showing boundary layers: (*a*) ψ_1 (the maximum streamfunction contour is 6.187); (*b*) θ_1 (the maximum isotherm is 0.1371); (*c*) ψ_2 (the maximum streamfunction is 1.378); (*d*) θ_2 (the maximum isotherm is 3.986×10^{-2}).

at a particular value of Ra the cold region is symmetrically placed over the hot region so that whatever heat is given up to, say, the left wall in the hot region is reabsorbed in the cold region and the net heat transfer over the length of the wall is zero. The particular value of Ra at which Nu_2 is zero has been estimated to be $Ra = 1200$. Beyond this value of the Rayleigh number, the distortion continues, causing the correctional Nusselt number, Nu_2, to change sign. At extremely high Ra thermal boundary layers form. In figure 9(*a–d*) we show ψ_1, θ_1, ψ_2, θ_2 at $Ra = 10^6$ where the boundary-layer behaviour can clearly be seen. We will discuss this further in §4.3.

Figure 10(*a*, *b*) shows logarithmic plots of the scaling of the streamfunction and temperature fields versus Ra. Figure 10(*a*) shows the absolute maximum of the streamfunctions, $|\psi_0|_{max}$, $|\psi_1|_{max}$ and $|\psi_2|_{max}$ as a function of the Rayleigh number. From the figure it is clear that there are two distinct regimes. For low Rayleigh numbers it is seen that $\psi_0 \sim Ra$, $\psi_1 \sim Ra$, and $\psi_2 \sim Ra^3$, but as $Ra \to \infty$ all three fields, ψ_0, ψ_1, ψ_2 have a $Ra^{1/4}$ dependence. From figure 10(*b*) similar observations can be made about the scaling of θ_0, θ_1 and θ_2 fields. θ_0 is always order unity. It is seen that $\theta_1 \sim Ra$ at low Rayleigh numbers but as $Ra \to \infty$, it becomes independent of Ra, i.e. it is $O(1)$. The θ_2 field scales as Ra^2 for low Ra but again becomes $O(1)$ as $Ra \to \infty$.

It is clear from figure 10 that the six variables, ψ_0, ψ_1, ψ_2 and θ_0, θ_1, θ_2, show two distinct scaling regimes and spatial structures at high and low Ra. By rescaling these

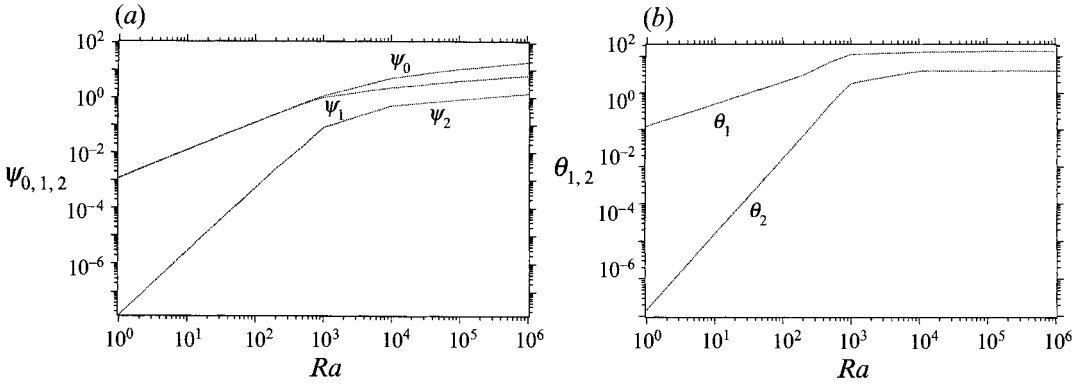

FIGURE 10. (*a*) Log-scale plot of $|\psi_0|_{max}$, $|\psi_1|_{max}$, $|\psi_2|_{max}$ *vs.* *Ra* showing the two scaling regimes. (*b*) Log-scale plot of $|\theta_1|_{max}$, $|\theta_2|_{max}$ *vs.* *Ra*.

fields in each regime, it is possible to cast the equations into parameter-free form which then elucidates the physics in each regime. In the next two subsections we consider the limits $Ra \ll 1$ and $Ra \to \infty$ respectively to determine the scaling behaviour.

4.2. *The small Ra and moderate Ra regimes*

In the previous subsection we noted significant structural changes as *Ra* is increased: the quadrupole streaming structure seen at low *Ra* disappears as *Ra* is increased; highly symmetric temperature fields also distort with increase in *Ra* leading to the interesting reversal in the direction of the heat transfer at $O(\epsilon^2)$. Some of these effects can be seen directly by examining the right-hand sides of (9)–(12). We will examine these in greater detail by considering expansions in *Ra* which will also explain the scalings seen in figure 10. Thus, for $Ra \ll 1$ we can expand the streamfunction and temperature fields in powers of Rayleigh number as follows:

$$\psi_i = \psi_{i0} + Ra\psi_{i1} + Ra^2\psi_{i2} + \ldots, \tag{20}$$

$$\theta_i = \theta_{i0} + Ra\theta_{i1} + Ra^2\theta_{i2} + \ldots, \tag{21}$$

where $i = 0, 1, 2$ represents the order of the field $O(\epsilon^i)$. Thus the problem is considered in the double limit $\epsilon \to 0, \omega \to 0$. Since both limits are regular expansions, it is easy to show that the double-parameter expansion implied by (20) and (21) is uniform and captures the leading terms regardless of the order in which the limits are taken. Substituting these expansions in (5), (6) and (9)–(12) and collecting terms of $O(Ra^0)$ it is seen that $\psi_{00} = \psi_{10} = \psi_{20} = 0$; similarly for the temperature fields it is easy to show that $\theta_{00} = 1 - x$; and $\theta_{10} = \theta_{20} = 0$. For $O(Ra)$ terms, we obtain the following equations for the stream functions: $\nabla^4\psi_{01} = -1$; $\nabla^4\psi_{11} = -1$ and $\nabla^4\psi_{21} = 0$. Since the boundary conditions are all homogeneous this shows that $\psi_0 \sim Ra$ and $\psi_1 \sim Ra$ and both fields correspond to a viscous circulation driven by a constant (uniform) vorticity source (Batchelor 1954). Similarly, for θ_{11} and θ_{21} we have

$$\nabla^2\theta_{11} = \boldsymbol{U}_{11} \cdot \nabla\theta_{00} = -\psi_{11y} \tag{22}$$

and $\nabla^2\theta_{21} = 0$, where the convective terms are written in terms of primitive variables. The boundary conditions are homogeneous. Equation (22) shows that $\theta_1 \sim Ra$ and the symmetries in the field ψ_{11} fully account for the vertical symmetry in θ_1, as seen in figure 2. In order to get the scaling for ψ_2 and θ_2 we consider the $O(Ra^2)$ terms, which give the following set of equations:

$$\nabla^4\psi_{22} = \tfrac{1}{2}\theta_{11x}, \tag{23}$$

$$\nabla^2\theta_{22} = \tfrac{1}{2}\boldsymbol{U}_{11} \cdot \nabla\theta_{11} + \boldsymbol{U}_{22} \cdot \nabla\theta_{00}, \tag{24}$$

Term	$Ra = 200$	$Ra = 10^3$
$U_1 \cdot \nabla\theta_1$	10^{-3}	10^{-1}
$U_1 \cdot \nabla\theta_0$	10^{-1}	10^{-1}
$U_1 \cdot \nabla\theta_1$	10^{-3}	10^{-1}
$U_2 \cdot \nabla\theta_0$	10^{-4}	10^{-1}
$U_0 \cdot \nabla\theta_2$	10^{-4}	10^{-2}

TABLE 7. Comparison of the orders of magnitude of the convection terms

with homogeneous boundary conditions showing that $\psi_2 \sim Ra^2$ and $\theta_2 \sim Ra^2$. All the scalings derived above seem to confirm those shown in figure 10, except ψ_2 which in figure 10(*a*) shows a Ra^3 scaling. This indicates that Ra expansion of ψ_2 is numerically dominated by the next-order term in Ra, ψ_{23}.

It is possible to use these expansions to understand some of the features of the steady-streaming flow at low Ra. As (23) indicates, the streaming is governed by the source term $\frac{1}{2}\theta_{11x}$. By examining the symmetries in θ_1 (by considering either (22) or figure 2), it is clear that $\frac{1}{2}\theta_{1x}$ changes sign in the four quadrants of the cavity, accounting for the quadrupole structure of the streaming flow observed. The field θ_{22} satisfying (24) is not so easy to interpret because it is not clear *a priori* which, if either, of the two source terms is more important, but the numerical results clearly show that it is $U_{11} \cdot \nabla\theta_{11}$. This term changes sign across the vertical midplane of the cavity leading to the antisymmetric distribution of isotherms observed in figure 4.

For moderate Ra where expansions in Ra are inaccurate, but before the occurrence of boundary-layer behaviour we have to consider the full equations (9)–(12). In particular we are interested in understanding the distortion of the θ_1 and θ_2 fields which causes a change in the sign of the correctional Nusselt number Nu_2. Therefore we consider (10) and (12) where it is again not clear which of the convective transport terms on the right-hand side are dominant. Table 7 shows the order of magnitude of each of these terms at two selected Rayleigh numbers, $Ra = 2 \times 10^2$ and 10^3. These order-of-magnitude estimates have been made by using the maximum value of each field over the domain. Considering $Ra = 2 \times 10^2$ first, in (10) it is clear from the table that $U_1 \cdot \nabla\theta_0$ dominates $U_0 \cdot \nabla\theta_1$. Similarly in (12), $U_1 \cdot \nabla\theta_1$ dominates the other terms. Figure 11(*a*, *b*) shows contours of the dominant source terms of (9) and (12), $U_1 \cdot \nabla\theta_0$ and $U_1 \cdot \nabla\theta_1$, at $Ra = 1$ and 2×10^2. It is clear from the figure that, as Ra is increased, the contours of the dominant source terms are rotated (albeit slightly) about the centre of the cavity leading to the distortion of the θ_1 and θ_2 fields. This argument can be extended to higher Rayleigh numbers but as can be seen from table 7, at high Ra, it is difficult to single out any single terms on the right-hand side as the dominant one and hence the physics here is more complex.

4.3. *High Rayleigh numbers and boundary-layer formation*

It is well known that natural convection in a cavity shows boundary-layer behaviour at the sidewalls as $Ra \to \infty$. Gill (1966) has considered convection in a cavity with a steady gravitational field, which corresponds to our $O(\epsilon^0)$ problem and developed scaling laws for the boundary layer. The streamfunction ψ_0 scales as $Ra^{1/4}$, and the boundary-layer thickness $\delta_0 \sim Ra^{-1/4}$. The boundary-layer equations are obtained by utilizing these scalings. The solution at the edge of the boundary layer matches the core solution which is a function of the longitudinal variable y only. Since the boundary-layer limit, $Ra \to \infty$ is a singular perturbation problem, we need to be concerned about

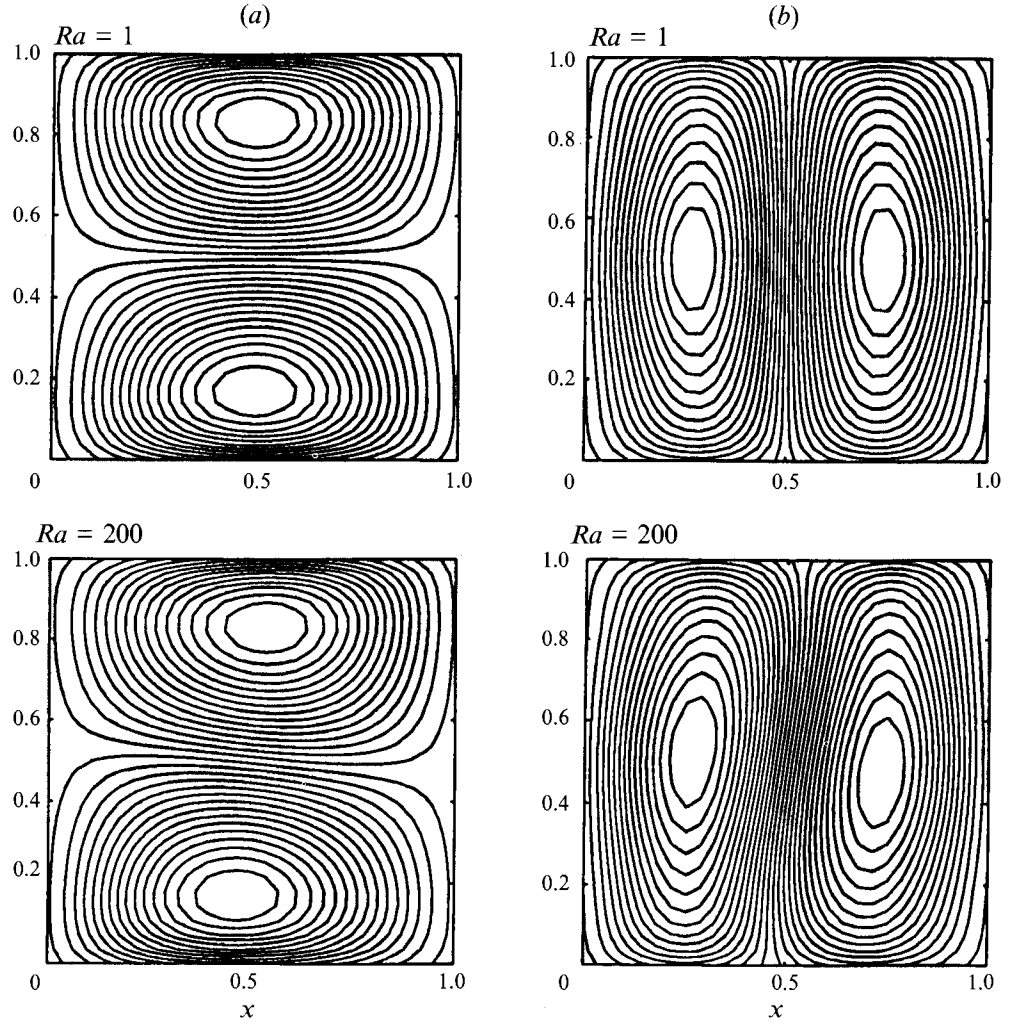

FIGURE 11. (*a*) Comparison of forcing term, $U_1 \cdot \nabla\theta_0$ at $Ra = 1$ and $Ra = 2 \times 10^2$. It can be seen that the forcing shows the same symmetry about the horizontal midplane at $Ra = 1$ as the θ_1 field (figure 2). Note a slight clockwise distortion of the $U_1 \cdot \nabla\theta_0$ field at $Ra = 200$, which can also be seen in the θ_1 field (figure 6*a*). (*b*) Comparison of $U_1 \cdot \nabla\theta_1$ at $Ra = 1$ and $Ra = 2 \times 10^2$. At $Ra = 1$ the $U_1 \cdot \nabla\theta_1$ field shows a symmetry about the vertical midplane like the θ_2 field. Similar to (*a*), note distortion of the $U_1 \cdot \nabla\theta_1$ at $Ra = 200$ field which accounts for the distortion of the θ_2 field (figure 8*a*).

the limit process $\epsilon \to 0, Ra \to \infty$ yielding a result different from that obtained by interchanging the limits.

Figure 10(*a*) confirms the $Ra^{1/4}$ dependence of our numerical solution of the ψ_0 field. It also shows that the ψ_1 and ψ_2 fields have the same scaling. This can be derived from the equations as well. Consider the $O(\epsilon)$ equations in the limit Ra, $Pr \to \infty$ and $\omega \to 0$:

$$\nabla^4\psi_1 = Ra\,\partial_x(\theta_0 + \theta_1), \quad \nabla^2\theta_1 = J(\psi_0, \theta_1) + J(\psi_1, \theta_0).$$

The scale of $O(\epsilon^0)$ fields is known. If the $O(\epsilon)$ boundary-layer thickness is assumed to be δ_1, we still have to determine the scales of ψ_1 and θ_1. The equations represent a linear system with homogeneous boundary conditions and a forcing term, $Ra\,\partial_x\theta_0$, which goes to zero at a distance δ_0 away from the wall. This leads us to conclude that ψ_1, θ_1

exhibit a boundary-layer structure of the same scale as δ_0. With this it is relatively simple to show that $\psi_1 \sim Ra^{1/4}$ and $\theta_1 \sim O(1)$. A similar analysis can be done at $O(\epsilon^2)$ to show that $\psi_2 \sim Ra^{1/4}$ and $\theta_2 \sim O(1)$.

We now rescale the variables to put the equations in parameter-free form: $X = xRa^{1/4}$; $Y = y$; $\tilde{\psi}_i(X, Y) = \psi_i / Ra^{1/4}$ and $\tilde{\theta}_i(X, Y) = \theta_i$, where $i = 0, 1, 2$ denotes the fields at $O(\epsilon^i)$. When these are inserted into (5), (6) and (9)–(12) in the limit Ra, $Pr \to \infty, \omega \to 0$, the equations of momentum and energy yield

$$\tilde{\psi}_{iXXX} = \sum_{k=0}^{i} a_k(\tilde{\theta}_i - \tilde{\theta}_i^c(Y)), \tag{25}$$

$$\theta_{iXX} = \sum_{k=0}^{i} a_k \tilde{J}(\tilde{\psi}_{i-k}, \tilde{\theta}_i), \tag{26}$$

where $\tilde{J}(U, V) = U_Y V_X - U_X V_Y$ and

$$a_k = \begin{cases} 1 & \text{if} \quad k = 0, 1 \\ \frac{1}{2} & \text{if} \quad k = 2. \end{cases}$$

We have integrated the momentum equation once with respect to X and the integration function, $\tilde{\theta}_i^c(Y)$ gives the temperature distribution in the core of the cavity, i.e. at $X \to \infty$. The boundary conditions for $\tilde{\psi}_i$ are the usual impermeability and no slip at the wall given by $\tilde{\psi}_i(0, Y) = 0$, $\tilde{\psi}_{iX}(0, Y) = 0$. The third boundary condition is that $\tilde{\psi}_i(\infty, Y) = \tilde{\psi}_i^c$ where $\tilde{\psi}_i^c$ is the streamfunction at the core. The temperature boundary conditions are $\tilde{\theta}_i(0, Y) = 1$ for $i = 0$ and $\tilde{\theta}_i(0, Y) = 0$ for $i = 1, 2$. The second boundary condition comes from assuming a known imposed temperature profile at $X \to \infty$, $\tilde{\theta}_i(\infty, Y) = \tilde{\theta}_i^c(Y)$. The boundary-layer equations represent a parabolic system that can in principle be integrated by marching along Y, with an iterative procedure used to determine the core variables, see e.g. Walker & Homsy (1980).

These equations provide insight into the boundary-layer structure: $\tilde{\psi}_{iXXX}$ denotes the gradient of vorticity at $O(\epsilon^i)$. Thus (25) conveys that the gradient of vorticity at any point within the boundary layer depends only on the difference between the local and core temperatures. Since all vorticity gradients vanish when the temperature equals the core temperature, the vorticity boundary layer is also of the same order of magnitude as the thermal boundary layer. Hence the flow in the cavity at high Ra at each order in ϵ exhibits the same boundary-layer structure as the base flow. It is easy to show that, as a consequence of the boundary-layer equations (25) and (26) with associated matching conditions, the scalings and equation hierarchies are identical to those obtained by the limiting process $Ra \to \infty, \epsilon \to 0$. Our numerical results are in agreement with this general picture. Figure 9 shows the $O(\epsilon)$ and $O(\epsilon^2)$ fields at $Ra = 10^6$, in which steep gradients exist within the boundary layer close to the lateral walls, while the fields in the core of the cavity are a function of y only.

5. Finite frequency

So far we have considered the case of large Prandtl numbers and vanishingly small forcing frequencies, which allowed us to focus on streaming due to thermal convection effects only. We now relax these assumptions to include the effect of inertia by considering finite Prandtl numbers and frequencies.

As discussed in detail above, there are potential resonances with the eigenstates of (13) and (14) which have been identified with the distinct modes of boundary layer and internal waves respectively. We are interested in conditions under which one or both

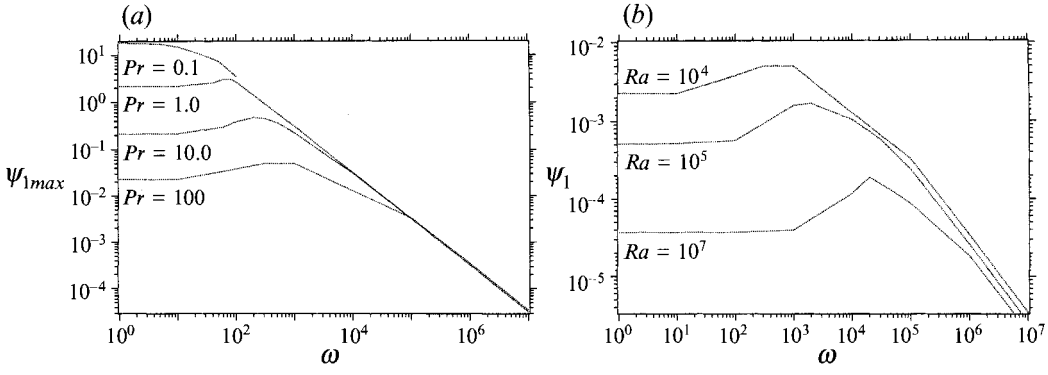

FIGURE 12. (*a*) Log-scale plot of ψ_1 *vs* ω at $Ra = 10^4$ and various Pr. (*b*) Log-scale plot of ψ_1 *vs* ω at $Pr = 100$ and various Ra.

modes are excited. Hence we have a multi-parameter multi-mode problem where we consider the effect of Ra, Pr and forcing frequency ω on the two possible modes of instability. In the following subsection we examine the $O(\epsilon)$ solutions for which resonances are possible, and in the next one we consider the resulting streaming fields.

5.1. $O(\epsilon)$ *fields*

We consider the solutions of (9) and (10). To begin with, some general features of the solution can be understood by examining the maximum values of ψ_1 and θ_1 in the cell as the parameters Ra, Pr and ω are varied. Let us fix Ra at 10^4 and examine the effect of ω and Pr in figure 12(*a*), which shows the maximum value of the scaled $O(\epsilon)$ streamfunction ψ_1/Pr plotted as a function of the forcing frequency ω, on a log-log plot. Several values of Pr are shown giving a family of curves. Many things can be noted from the figure. (i) For low frequencies all the curves are relatively flat and asymptote to the zero-frequency limit results of §4. (ii) Curves for different Pr collapse for high ω confirming a $\psi_1 \sim Pr/\omega$ scaling which can readily be derived from (9) and (10) in the asymptotic limit $\omega \to \infty$. (iii) For $Pr > 1$ the streamfunction has a mild resonance seen in the hump of the curve; for $Pr \ll 1$ no resonance can be seen. The flow shows a broad resonant interaction and we call the frequency corresponding to the peak of the curve the resonant frequency. We note that at fixed Ra the resonant frequency shows the scaling $\omega \sim Pr^{1/2}$ for $Pr > 1$. The θ_1 field shows similar behaviour; however, the resonance is very weak.

At low frequency, in the quasi-static limit, the system gives a forced periodic response. As $\omega \to \infty$ the system is unable to respond and this is seen in the high-frequency roll-off noted. Only at intermediate frequencies is a resonant response possible. Recall that the Brunt–Väisälä frequency ω_{BV} associated with the internal wave is given in our scaling by

$$\omega_{BV} = (\gamma Ra\, Pr)^{1/2}, \tag{27}$$

where γ is the stratification parameter in the core of the cavity, defined by $\gamma = \theta_{0y}$. The Brunt–Väisälä frequency represents the highest frequency oscillation that any stratified medium can support, hence no internal waves of higher frequency can be excited, which explains the asymptotic roll-off that is observed.

Next we hold Pr constant and investigate the effect of Ra. In figure 12(*b*) the maximum streamfunction versus ω curves are shown for $Ra = 10^4$, 10^5 and 10^7 at $Pr = 100$. The scaling of the y-axis is $\psi_1/Ra^{3/4}$. We note that the curves show the same general features that were pointed out earlier in figure 12(*a*). However, as Ra is

Ra	Pr	ω_{max}	$\omega_{max}/(Ra\,Pr)^{1/2}$
10^4	1	60	0.6
10^4	10	200	0.63
10^4	100	600	0.6
10^5	100	2000	0.63
10^7	100	20000	0.63

TABLE 8. The observed resonant frequency for various Ra and Pr and the calculated stratification parameter

increased, the strength of the resonant response also increases, and the band width of interaction becomes narrower.

Other features seen from figure 12(b) include the collapsing of the curves for different Ra in the limit $\omega \to \infty$ which confirms the correctness of the $\psi_1 \sim Ra^{3/4}$ scaling. What cannot be seen from figure 12 is that, at low frequencies, the response of the system as measured by its maximum value over the domain is in temporal phase with the applied forcing. However, as the frequency is increased the phase changes, and in the limit $\omega \to \infty$, the fields are $\frac{1}{2}\pi$ out of phase with the forcing. This can easily be seen from the equations, because at high frequencies diffusion of vorticity can be ignored and the rate of production of vorticity is balanced by its temporal rate of change. Thus if we assume that boundary-layer thickness $\delta_1 \sim Ra^{-1/4}$ (discussed earlier) we have $\psi_1 \sim \mathrm{i}Ra^{3/4}Pr/\omega$.

Our results are in excellent agreement with the scaling implied by (27). Table 8 gives the values of the frequency at which the amplitude of the $O(\epsilon)$ fields is a maximum, over a range of Ra and Pr. As can be seen, they obey the approximate relation

$$\omega \approx 0.62(Ra\,Pr)^{1/2}$$

over $10^4 \leqslant Ra \leqslant 10^7$, and $1.0 \leqslant Pr \leqslant 100$. The apparently high value of the effective stratification parameter implied by the results ($\gamma \approx 0.8$) as opposed to the conventional value of 0.5 may be explained as follows. The local stratification at the top and bottom of the cavity is likely to be most relevant, since it is here that the internal waves are excited by the turning boundary-layer flow, and the stratification there in turn is well known to be larger than in the middle of the core where the value 0.5 pertains. Thus there is good evidence from the scaling behaviour that an internal gravity wave is being excited.

We can also analyse the detailed field information for ψ_1, θ_1 over the domain and look for gravity waves. Consider figure 13, where we show a time sequence of the $O(\epsilon)$ field $\psi_1(x, \phi) = \psi_1'^R \cos(\phi) - \psi_1'^I \sin(\phi)$ where $\phi = \omega\tau$ denotes the phase of the sinusoidally oscillating field as ϕ varied from 0 to π, with increments of $\pi/8$. The overall picture that emerges is that when the $O(\epsilon^0)$ hot (cold) fluid turning at the upper left (lower right) corner of the cavity is subjected to sinusoidal excitation, it excites

FIGURE 13. Time sequence of ψ_1 at $Ra = 10^7$ and $Pr = 100$ from $\phi = 0$ to π at intervals of $\pi/8$. The maximum value of the streamfunction, ψ_{max} and the value at the centre of the cavity, ψ_{mid} are (a) at $\phi = 0$: $\psi_{max} = -22.86$, $\psi_{mid} = -18.901$: (b) at $\phi = \pi/8$: $\psi_{max} = \psi_{mid} = -28.106$; ($c$) at $\phi = \pi/4$: $\psi_{max} = \psi_{mid} = -33.032$; ($d$) at $\phi = 3\pi/8$: $\psi_{max} = \psi_{mid} = -32.929$; ($e$) at $\phi = \pi/2$: $\psi_{max} = \psi_{mid} = -27.812$; ($f$) at $\phi = 5\pi/8$: $\psi_{max} = \psi_{mid} = -18.462$; ($g$) at $\phi = 3\pi/4$: $\psi_{max} = 16.253$, $\psi_{mid} = -6.301$; (h) at $\phi = 7\pi/8$: $\psi_{max} = 20.978$, $\psi_{mid} = 8.421$.

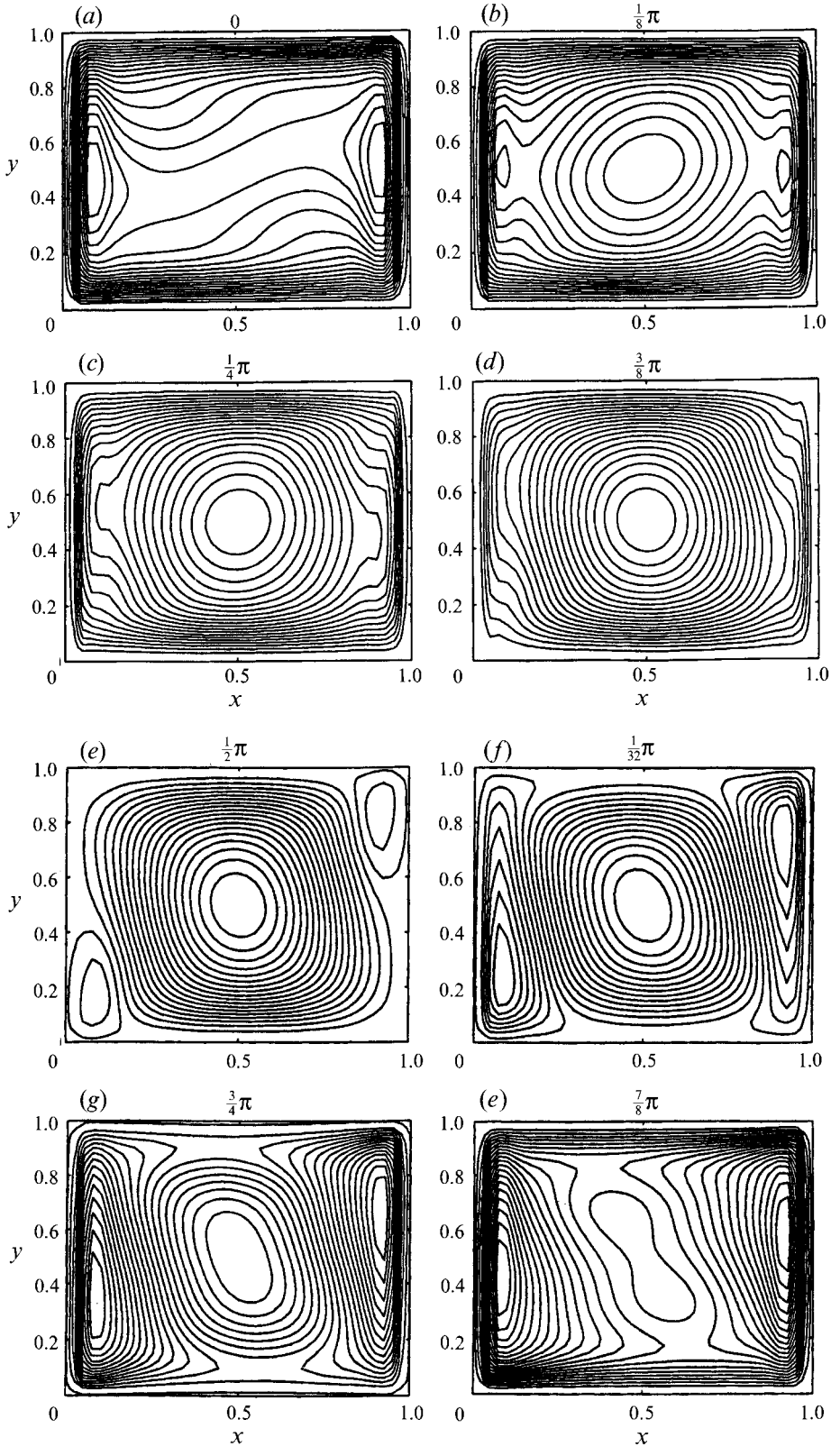

FIGURE 13. For caption see facing page.

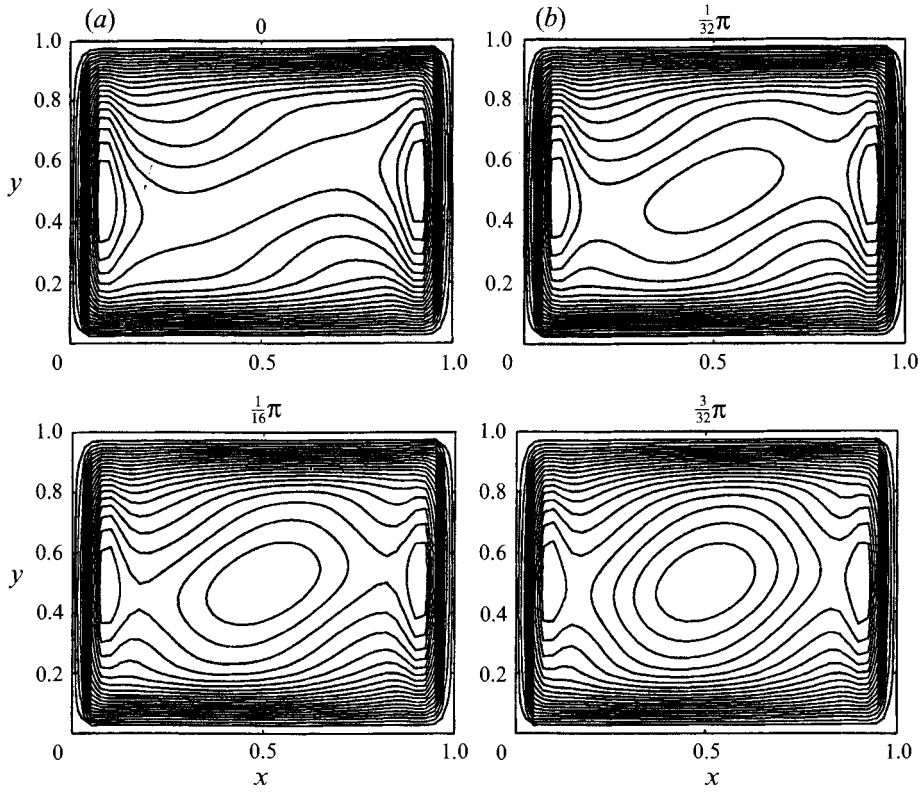

FIGURE 14. Time sequence of ψ_1 at $Ra = 10^7$ and $Pr = 100$ from $\phi = 0$ to $\pi/8$ at intervals of $\pi/32$: (*a*) at $\phi = 0$: $\psi_{max} = -22.86$, $\psi_{mid} = -18.901$; (*b*) at $\phi = \pi/32$: $\psi_{max} = -22.86 = \psi_{mid} = -21.536$; (*c*) at $\phi = \pi/16$: $\psi_{max} = \psi_{mid} = -23.964$; (*d*) at $\phi = 3\pi/32$: $\psi_{max} = \psi_{mid} = -26.161$.

travelling waves that travel to the opposite right (left) wall. In the centre of the cavity the two waves engage in constructive/destructive interference leading to the formation of a stationary wave. At $\phi = 0$, as the figure shows, we see two wave packets, at the upper right and lower left corners. Since the evolution at this stage is rapid we have shown in figure 14 a time sequence at phase intervals of $\frac{1}{32}\pi$ between $\phi = 0$ and $\frac{1}{8}\pi$. As the wave packets move towards the centre of the cavity, interference takes place leading to the formation of a stationary wave (seen in the closed elliptic curves) at $\phi = \frac{1}{16}\pi$. Then as the cycle proceeds, this standing wave grows and engulfs the entire cavity, seen at $\phi = \frac{3}{8}\pi$. Then, by mechanisms that are not entirely clear, eddies form in the lower left (and upper right) corners of the cavity that gain in strength as the cycle proceeds. The growth of these eddies is at the expense of the standing wave which begins to shrink and is finally completely extinguished by the eddies. A very weak wave flanked by strong circulations on either side is seen at $\phi = \frac{7}{8}\pi$. How is the wave re-formed? This evolution is also rapid and hence we consider a time sequence at intervals of $\frac{1}{32}\pi$ from $\phi = \frac{7}{8}\pi$ to π. These are shown in figure 15, and as can be seen at $\phi = \frac{29}{32}\pi$, only a small vestige of the wave remains, but new disturbances are excited that grow rapidly and soon the eddies on the sidewall recede, leading to the scenario that was presented at $\phi = 0$. This is again repeated in the other half of the cycle, from $\phi = \pi$ to 2π.

In figure 16 we show the temperature field θ_1 for $\phi \in (0, \pi)$ at intervals of $\frac{1}{8}\pi$. It may be recalled that the temperature field does not show a significant resonant response.

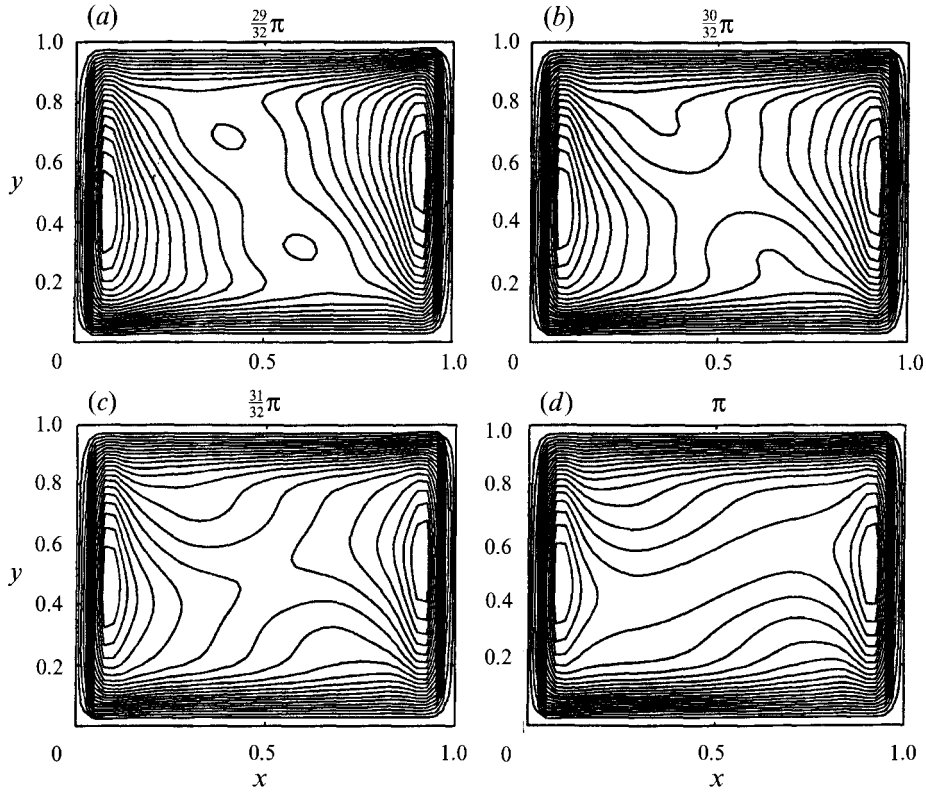

FIGURE 15. Time sequence of ψ_1 at $Ra = 10^7$ and $Pr = 100$ from $\phi = 7\pi/8$ to π at intervals of $\pi/32$: (*a*) at $\phi = 29\pi/32$: $\psi_{max} = 21.745$, $\psi_{mid} = 10.014$; (*b*) at $\phi = 30\pi/32$: $\psi_{max} = 22.324 = \psi_{mid} = 13.112$; (*c*) at $\phi = 31\pi/32$: $\psi_{max} = 22.701$, $\psi_{mid} = 16.0845$; (*d*) at $\phi = \pi$: $\psi_{max} = 22.86$, $\psi_{mid} = 18.901$.

The figure shows that the temperature field is dominated by the boundary layers, and the response to the forcing is quite weak. However, a wave-like mode does form and from the sequence shown is strongest at $\phi = \frac{7}{8}\pi$. There are some interesting features that we wish to point out. The temperature field is approximately $\frac{1}{2}\pi$ out of phase with the velocity (streamfunction) field, because when the velocity 'wave' is at its peak, at $\phi = \frac{1}{2}\pi$, temperature 'wave' is at its minimum, and the temperature field only shows boundary layers. And when the temperature wave is strongest, $\phi = \frac{7}{8}\pi$ the velocity 'wave' is at its weakest. This is not a coincidence, but a result of the property of small-amplitude waves that they transport only momentum, not mass. This property can serve as a useful diagnostic tool which in our case confirms that the features seen in figures 13–16 are indeed waves and not just the response to forced oscillations.

We thus conclude that for the range of parameters (Ra, Pr, ω) considered there is an interaction with the internal gravity wave. There is no evidence of any interaction with the boundary-layer instability but this is probably because the Ra considered is too low: from (15), at $Pr = 100$, the critical Rayleigh number for neutral boundary-layer waves Ra_{BL}, is 4.176×10^8, which is much higher than the highest Rayleigh number (10^7) that we have considered. It may be argued that Ra_{BL} can be lowered by choosing sufficiently small Pr. We note however that (15) was derived for the stability of a model boundary-layer problem, that of convection in a slot. In the present case of flow in a cavity, the separation of flow into two regimes and the formation of boundary layers is highly dependent on the Prandtl number. If the Prandtl number is small the

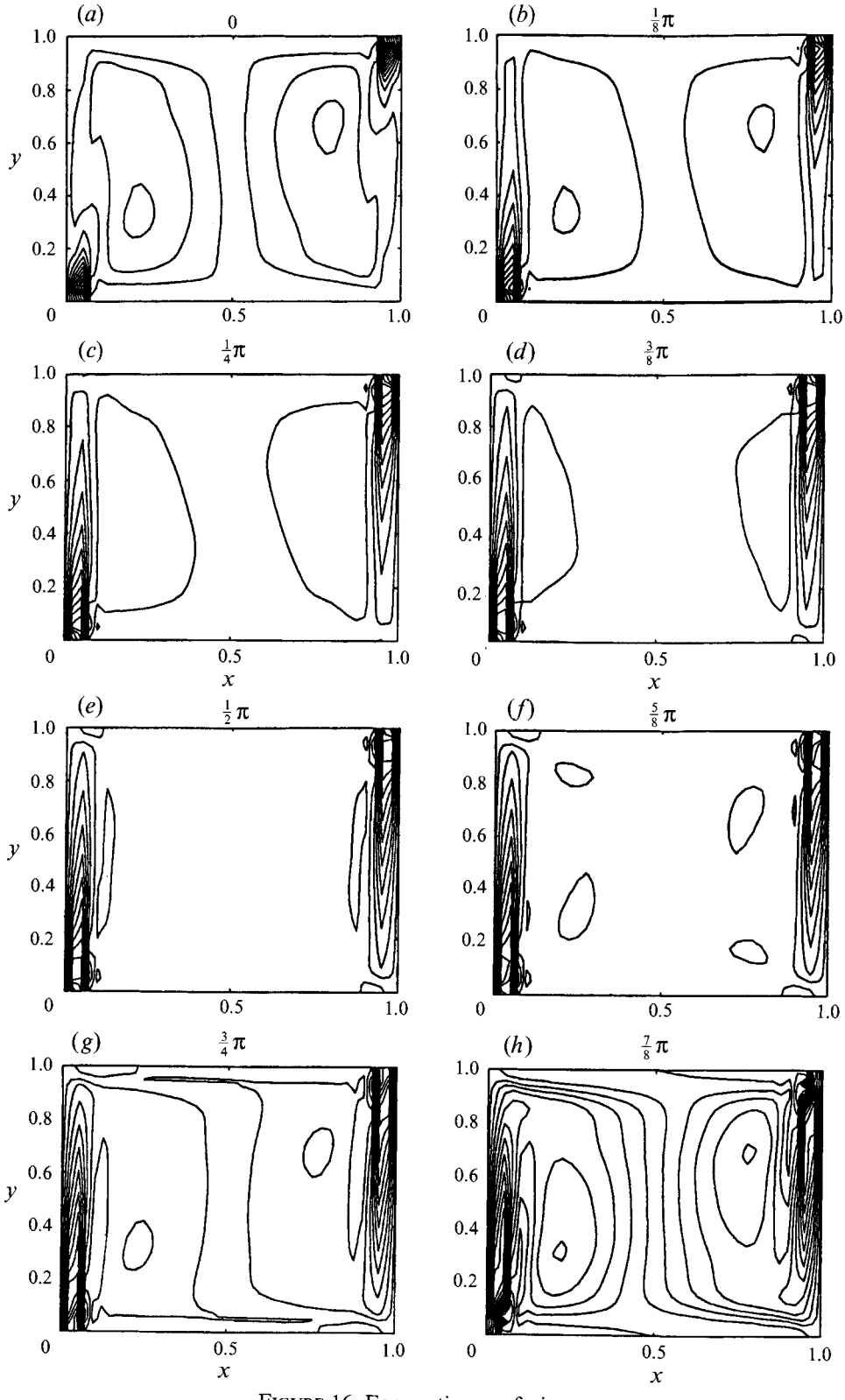

FIGURE 16. For caption see facing page.

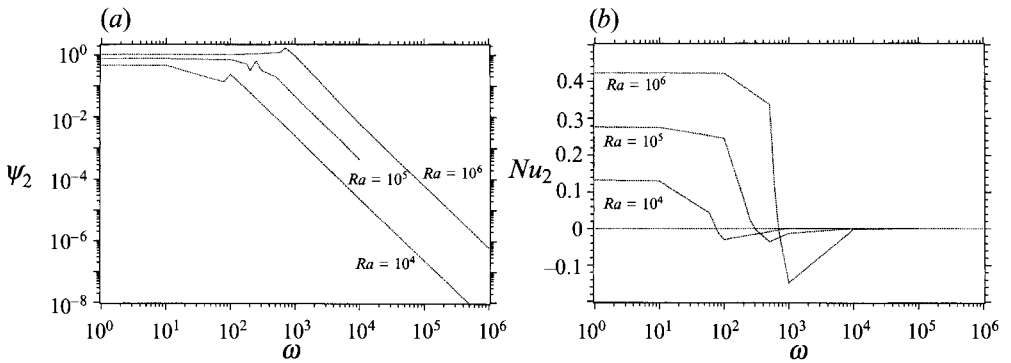

FIGURE 17. (*a*) Log-scale plot of ψ_2 *vs.* ω at $Pr = 1$ and various Ra. (*b*) Plot of Nu_2 *vs* ω for various Ra at $Pr = 1$ showing the change in sign of Nu_2. Note that the value of ω at which the sign changes corresponds to the frequency of the internal gravity wave.

temperature field is essentially conductive, indicating that modes associated with vertical stratification will not be present.

5.2. *Streaming flow*

We now consider whether the resonant responses of the $O(\epsilon)$ fields can lead to large changes in the streaming response. The streaming flow is governed by the following forcing terms. In the vorticity transport equation we have forcing due to convection of vorticity, $(1/2Pr)[J(\psi_1^R, \nabla^2\psi_1^R) + J(\psi_1^I, \nabla^2\psi_1^I)]$, and forcing due to production of vorticity due to buoyancy, $\frac{1}{2}Ra\,\partial_x\theta_1$. In the energy equation the forcing is due to convective transport of energy, $\frac{1}{2}[J(\psi_1^R, \theta_1^R) + J(\psi_1^I, \theta_1^I)]$. As we noted previously, the θ_1 response has no structure, hence the buoyancy forcing can show no resonance. The Reynolds-stress terms (from the convection of vorticity) do show resonance since they are associated with the internal wave, but the strength of the forcing is itself dependent on Prandtl number, approximately $\sim 1/Pr$. Thus we expect that for $Pr \gg 1$ there would be no effect because the forcing goes to zero. For $Pr \ll 1$, we do not expect any resonance because there is no stratification to begin with and hence no internal waves can be formed. Thus it seems that $Pr = 1$ would show maximum effect. This is indeed borne out by our calculations for ψ_2 which show a resonant response near $Pr = 1$. Figure 17(*a*), which plots the order of magnitude of the streaming flow stream-function versus the forcing frequency for $Ra = 10^4$, 10^5, 10^6 at $Pr = 1$, shows this resonant response. It should however be noted that the resonances get stronger as Ra is increased implying that these effects could become significant at $Ra \gg 10^6$. At high frequencies the streaming flow also decays rapidly, as $1/\omega^2$.

Another interesting effect concerns the Nusselt number, Nu_2. Figure 17(*b*) shows a plot of Nu_2 *vs.* ω for various Ra at $Pr = 1.0$. It can be seen that Nu_2 falls sharply near ω_{BV} and changes sign. This is very easily explained when one considers the forcing term in the energy equation, $\mathrm{Re}[J(\psi_1, \theta_1)]$. We have noted before that the phase difference between temperature and streamfunction becomes $\frac{1}{2}\pi$ at resonance, and hence the time average of the forcing term above goes to zero, leading to the drop in Nu_2.

FIGURE 16. Time sequence of θ_1 at $Ra = 10^7$ and $Pr = 100$ from $\phi = 0$ to π at intervals of $\pi/8$. The maximum value of the isotherms is: (*a*) at $\phi = 0$: $\theta_1 = 13.0 \times 10^{-3}$; (*b*) at $\phi = \pi/8$: $\theta_1 = 21.1 \times 10^{-3}$; (*c*) at $\phi = \pi/4$: $\theta_1 = 25.9 \times 10^{-3}$; (*d*) at $\phi = 3\pi/8$: $\theta_1 = 26.8 \times 10^{-3}$; (*e*) at $\phi = \pi/2$: $\theta_1 = 26.0 \times 10^{-3}$; (*f*) at $\phi = 5\pi/8$: $\theta_1 = 21.6 \times 10^{-3}$; (*g*) at $\phi = 3\pi/4$: $\theta_1 = 14.5 \times 10^{-3}$; (*h*) at $\phi = 7\pi/8$: $\theta_1 = 6.8 \times 10^{-3}$.

6. Extension to general forcing

So far we have assumed that the time-dependent forcing is a simple harmonic function. It is fairly straightforward to investigate the effect of a more generalized forcing function $f(\tau)$ which, while being $O(\epsilon)$, spatially uniform and aligned with the steady gravitational field, has a more general dependence on time. Such a forcing has sufficient generality to raise the prospect of simultaneously exciting several modes of instability.

Since the governing equations are linear, it is possible to solve the $O(\epsilon)$ flow for each of the Fourier components of the forcing and then the flow can be reconstructed by summing together the Fourier components. For the streaming flow one now needs to consider the contribution of the nonlinear self-interaction of each of the above-mentioned $O(\epsilon)$ Fourier modes that contribute to time-averaged Reynolds-stress type of terms. We now show that these forcing terms for the streaming flow are a weighted function of the autocorrelation of the applied forcing.

Hence, considering a general forcing function $f(\tau)$, we have at $O(\epsilon)$

$$-\frac{1}{Pr}\partial_\tau(\nabla^2\psi_1)+\mathscr{L}_\psi(\psi_1,\theta_1)=Ra\,\partial_x\theta_0 f(\tau), \tag{28}$$

$$\partial_\tau\theta_1+\mathscr{L}_\theta(\psi_1,\theta_1)=0, \tag{29}$$

with boundary conditions as before, but here $\psi_1=\psi_1(x,y,t)$ and $\theta_1=\theta_1(x,y,t)$. Taking the Fourier transform of (28) and (29) defined as $\mathscr{F}:\tau\to s$, we denote the transformed variables as $\tilde{\psi}_1(x,y,s)$, $\tilde{\theta}_1(x,y,s)$ and $\tilde{f}(s)$. If the variables are rescaled as $\hat{\psi}_1(x,y,s)=\tilde{\psi}_1(x,y,s)/\tilde{f}(s)$ and $\hat{\theta}_1(x,y,s)=\tilde{\theta}_1(x,y,s)/\tilde{f}(s)$ we get for each mode s,

$$-\frac{\mathrm{i}s}{Pr}(\nabla^2\hat{\psi}_1)+\mathscr{L}_\psi(\hat{\psi}_1,\hat{\theta}_1)=Ra\,\partial_x\hat{\theta}_0, \tag{30}$$

$$\mathrm{i}s\hat{\theta}_1+\mathscr{L}_\theta(\hat{\psi}_1,\hat{\theta}_1)=0, \tag{31}$$

which are of course identical to (9) and (10) for the discrete-frequency case. The above equations give the solution for any mode s. The full solution at $O(\epsilon)$ (for say ψ_1) can be reconstructed by considering the inverse transform $\mathscr{F}^{-1}[\tilde{\psi}_1]=\mathscr{F}^{-1}[\hat{\psi}_1\tilde{f}(s)]$ which can also be expressed as the convolution product: $\psi_1=\bar{\psi}_1(\tau)*f(\tau)$, $\bar{\psi}_1(\tau)$ being the inverse transform of $\hat{\psi}_1$. Similar relations hold for θ_1.

At $O(\epsilon^2)$, we have the time-dependent equations

$$-\frac{1}{Pr}\partial_\tau(\nabla^2\psi_2)+\mathscr{L}_\psi(\psi_2,\theta_2)=Ra\,\partial_x\theta_1 f(\tau)+\frac{1}{Pr}J(\psi_1,\nabla^2\psi_1), \tag{32}$$

$$\partial_\tau\theta_2+\mathscr{L}_\theta(\psi_2,\theta_2)=J(\psi_1,\theta_1), \tag{33}$$

where again the boundary conditions are the same as before, and $\psi_2=\psi_2(x,y,t)$ and $\theta_2=\theta_2(x,y,t)$. Taking the Fourier transform of the above, it is seen that the right-hand side involves convolution products of $\tilde{\psi}_1(x,y,s)$, $\tilde{\theta}_1(x,y,s)$ and $\tilde{f}(s)$. Since it is only the steady-streaming terms that are of interest to us we consider $s=0$. Thus by making appropriate substitutions, it is easy to show (by recognizing that $f(\tau)$, ψ_1 and θ_1 are real valued), that the above equations can be written as

$$\mathscr{L}_\psi(\hat{\psi}_2,\hat{\theta}_2)=\int_{-\infty}^{\infty}E(\xi)\,\partial_x\hat{\theta}_1(x)\,\mathrm{d}\xi+\frac{1}{Pr}\int_{-\infty}^{\infty}E(\xi)\,J(\hat{\psi}_1(\xi),\nabla^2\hat{\psi}_1^*(\xi))\,\mathrm{d}\xi, \tag{34}$$

$$\mathscr{L}_\theta(\hat{\psi}_2,\hat{\theta}_2)=\int_{-\infty}^{\infty}E(\xi)\,J(\hat{\psi}_1(\xi),\hat{\theta}_1^*(\xi))\,\mathrm{d}\xi, \tag{35}$$

where $E(\xi) = \tilde{f}(\xi)\tilde{f}(-\xi) = \tilde{f}(\xi)\tilde{f}^*(\xi)$ is the spectral energy density. We have also used the fact that because these are real-valued functions, $\hat{\psi}_1^*(\xi) = \hat{\psi}_1(-\xi)$ and $\hat{\theta}_1^*(\xi) = \hat{\theta}_1(-\xi)$. In order to cast the equations in a form more akin to (11) and (12) we split each of the integrals as

$$\int_{-\infty}^{\infty} = \int_{-\infty}^{0} + \int_{0}^{\infty}.$$

If the transformed variables are split into real and imaginary parts, $\hat{\psi}_1(\xi) = \hat{\psi}_1^R(\xi) + \mathrm{i}\hat{\psi}_1^I(\xi)$, $\hat{\theta}_1(\xi) = \hat{\theta}_1^R(\xi) + \mathrm{i}\hat{\theta}_1^I(\xi)$, further manipulation results in

$$\mathscr{L}_\psi(\hat{\psi}_2, \hat{\theta}_2) = 2\int_0^\infty E(\xi)\left(\partial_x \hat{\theta}_1^R(\xi) + \frac{1}{Pr}(J(\hat{\psi}_1^R(\xi), \nabla^2\hat{\psi}_1^R(\xi)) + J(\hat{\psi}_1^I(\xi), \nabla^2\hat{\psi}_1^I(\xi))\right)\mathrm{d}\xi, \quad (36)$$

$$\mathscr{L}_\theta(\hat{\psi}_2, \hat{\theta}_2) = 2\int_0^\infty E(\xi)(J(\hat{\psi}_1^R(\xi), \hat{\theta}_1^R(\xi)) + J(\hat{\psi}_1^I(\xi), \hat{\theta}_1^I(\xi)))\,\mathrm{d}\xi. \quad (37)$$

It is interesting to note that in order to find the time-dependent $O(\epsilon)$ fields we need to know the full time-dependent forcing $f(\tau)$, but to compute the streaming flow only the spectral energy distribution is sufficient. Since one is not usually interested in the full time-dependent response but some mean characteristics of the flow, it is interesting to know that one need not know the full time-dependent forcing either: its spectral energy distribution is sufficient for statistical type of information about the flow.

Finally we point out that having solved (9) and (10) for a range of frequencies, we can easily compute the streaming for more complicated forcings. In particular the solution to (36) and (37) can be constructed by simply taking the weighted integral of ψ_2 with respect to the spectral energy density function.

The authors acknowledge the support of the US Dept. of Energy, Office of Basic Energy Sciences (Grant No. DE-FG03-87ER13673) and NASA Grant NAG-3-1475. We also thank Mr James Cross for doing some preliminary numerical computations.

REFERENCES

ALEXANDER, J. I. D. 1990 Low gravity experiment sensitivity to residual acceleration: A review. *Microgravity Sci. Technol.* **III** (2), 52–68.

ALEXANDER, J. I. D., AMIROUDINE, S., OUZZANI, J. & ROSENBERGER, F. 1991 Analysis of the low gravity tolerance of Bridgman–Stockbarger crystal growth II. Transient and periodic accelerations. *J. Cryst. Growth* **113**, 21–38.

AMIN, N. 1988 The effect of g-jitter on heat transfer. *Proc. R. Soc. Lond.* A **419**, 151–172.

BATCHELOR, G. K. 1954 Heat transfer by free convection across a closed cavity between vertical boundaries at different temperatures. *Q. Appl. Maths* **12**, 209–233.

BERGHOLZ, R. F. 1978 Stability of natural convection in a vertical fluid layer. *J. Fluid Mech.* **84**, 743–768.

BIRINGEN, S. & DANABASOGLU, G. 1990 Computation of convective flow with gravity modulation in rectangular cavities. *J. Thermophys.* **4**, 357–365.

BIRINGEN, S. & PELTIER, L. J. 1990 Computational study of 3-D Bénard convection with gravitational modulation. *Phys. Fluids* A **2**, 279–283.

CHENOWETH, D. R. & PAOLUCCI, S. 1986 Natural convection in an enclosed vertical air layer with large temperature horizontal temperature differences. *J. Fluid Mech.* **169**, 173–210.

ELDER, J. W. 1965 Laminar free convection in a vertical slot. *J. Fluid Mech.* **23**, 77–98.

GEBHART, B., JALURIA, Y., MAHAJAN, R. L. & SAMMAKIA, B. 1988 *Buoyancy Induced Flows and Transport.* Hemisphere.

GILL, A. E. 1966 The boundary layer regime for convection in a rectangular cavity. *J. Mech.* **26**, 515–536.

GILL, A. E. & DAVEY, A. 1969 Instabilities of a buoyancy-driven system. *J. Fluid Mech.* **35**, 775–798.

GRESHO, P. M. & SANI, R. L. 1970 The effects of gravity modulation on the stability of a heated fluid layer. *J. Fluid Mech.* **40**, 783–806.

IVEY, G. N. 1984 Experiments on transient natural convection in a cavity. *J. Fluid Mech.* **144**, 389–401.

LIGHTHILL, J. 1978 Acoustic streaming. *J. Sound Vib.* **61**, 391–418.

PAOLUCCI, S. & CHENOWETH, D. R. 1989 Transition to chaos in a differentially heated cavity. *J. Fluid Mech.* **201**, 379–410.

PATTERSON, J. & IMBERGER, J. 1980 Unsteady natural convection in a rectangular cavity. *J. Fluid Mech.* **100**, 65–86.

RAYLEIGH, LORD 1945 *The Theory of Sound.* Dover.

SCHLICHTING, H. 1979 *Boundary Layer Theory*, 7th edn. McGraw-Hill.

THORPE, S. A. 1968 On standing internal gravity waves of finite amplitude. *J. Fluid Mech.* **32**, 489–528.

VAHL DAVIS, G. DE 1968 Laminar convection in an enclosed rectangular cavity. *Intl J. Heat Mass Transfer* **11**, 1675–1693.

VAHL DAVIS, G. DE & JONES, I. P. 1982 Natural convection in a square cavity: A comparison exercise. *Rep.* 1982/FMT/3. School of Mechanical & Industrial Eng., The University of New South Wales, Kensington, Australia.

WALKER, K. L. & HOMSY, G. M. 1978 Convection in a porous cavity. *J. Fluid Mech.* **87**, 449–474.

ZLATEV, Z., WASNIEWSKI, J. & SCHAUMBURG, K. 1981 *Solution of Large and Sparse Systems of Linear Algebraic Equations.* Lecture Notes in Computer Science. Springer.